Monthly Notices
of the
ROYAL ASTRONOMICAL SOCIETY

MNRAS **499,** 2357–2379 (2020)
Advance Access publication 2020 September 3

doi:10.1093/mnras/staa2393

Blanco DECam Bulge Survey (BDBS) II: project performance, data analysis, and early science results

Christian I. Johnson [1]★ Robert Michael Rich [2] Michael D. Young,[3] Iulia T. Simion,[4] William I. Clarkson,[5] Catherine A. Pilachowski,[6] Scott Michael,[6] Andrea Kunder,[7] Andreas Koch[8] and Anna Katherina Vivas [9]

[1]*Space Telescope Science Institute, 3700 San Martin Drive, Baltimore, MD 21218, USA*
[2]*Department of Physics and Astronomy, UCLA, 430 Portola Plaza, Box 951547, Los Angeles, CA 90095-1547, USA*
[3]*Indiana University, University Information Technology Services, CIB 2709 E 10th Street, Bloomington, IN 47401 USA*
[4]*Key Laboratory for Research in Galaxies and Cosmology, Shanghai Astronomical Observatory, 80 Nandan Road, Shanghai 200030, China*
[5]*Department of Natural Sciences, University of Michigan-Dearborn, 4901 Evergreen Rd. Dearborn, MI 48128, USA*
[6]*Indiana University Department of Astronomy, SW319, 727 E 3rd Street, Bloomington, IN 47405 USA*
[7]*Saint Martin's University, 5000 Abbey Way SE, Lacey, WA 98503, USA*
[8]*Zentrum für Astronomie der Universität Heidelberg, Astronomisches Rechen-Institut, Mönchhofstr. 12, D-69120 Heidelberg, Germany*
[9]*Cerro Tololo Inter-American Observatory, NSF's National Optical-Infrared Astronomy Research Laboratory, Casilla 603 La Serena, Chile*

Accepted 2020 August 6. Received 2020 August 6; in original form 2019 December 9

ABSTRACT

The Blanco DECam Bulge Survey (BDBS) imaged more than 200 sq deg of the Southern Galactic bulge using the *ugrizY* filters of the Dark Energy Camera, and produced point spread function photometry of approximately 250 million unique sources. In this paper, we present details regarding the construction and collation of survey catalogues, and also discuss the adopted calibration and dereddening procedures. Early science results are presented with a particular emphasis on the bulge metallicity distribution function and globular clusters. A key result is the strong correlation ($\sigma \sim 0.2$ dex) between $(u-i)_o$ and [Fe/H] for bulge red clump giants. We utilized this relation to find that interior bulge fields may be well described by simple closed box enrichment models, but fields exterior to $b \sim -6^\circ$ seem to require a secondary metal-poor component. Applying scaled versions of the closed box model to the outer bulge fields is shown to significantly reduce the strengths of any additional metal-poor components when compared to Gaussian mixture models. Additional results include: a confirmation that the *u* band splits the subgiant branch in M22 as a function of metallicity, the detection of possible extratidal stars along the orbits of M 22 and FSR 1758, and additional evidence that NGC 6569 may have a small but discrete He spread, as evidenced by red clump luminosity variations in the reddest bands. We do not confirm previous claims that FSR 1758 is part of a larger extended structure.

Key words: Galaxy: bulge.

1 INTRODUCTION

The Galactic bulge has been a subject of intense spectroscopic and photometric investigation over the last 15 yr (e.g. see recent reviews by Rich 2013; Babusiaux 2016; McWilliam 2016; Nataf 2017; Barbuy, Chiappini & Gerhard 2018). Numerous lines of observational and theoretical evidence (e.g. McWilliam & Zoccali 2010; Nataf et al. 2010; Saito et al. 2011; Wegg & Gerhard 2013; Ness & Lang 2016; Portail et al. 2017; Simion et al. 2017) indicate that the central bulge is dominated by a boxy/peanut or 'X'-shape structure. Kinematic surveys have conclusively shown that the majority of bulge stars exhibit cylindrical rotation (Howard et al. 2009; Kunder et al. 2012; Ness et al. 2013b; Zoccali et al. 2014) consistent with properties found in 'pseudo-bulges' of other galaxies (e.g. Kormendy & Kennicutt 2004), and in fact the Milky Way may be an almost pure disc galaxy (Shen et al. 2010).

However, some metallicity-dependent kinematic differences, such as the presence (or not) of a vertex deviation (Soto, Rich & Kuijken 2007; Babusiaux et al. 2010) and differing orbital anisotropies (Clarkson et al. 2018), suggest that the Milky Way bar is predominantly supported by metal-rich stars. More metal-poor stars, especially outside ∼1 kpc from the Galactic centre, may represent a combination of inner halo or thick disc populations (e.g. Portail et al. 2017). A minor classical/merger-built bulge component has not yet been ruled out, and chemodynamic evidence from RR Lyrae stars in particular indicates that the oldest, most metal-poor bulge stars form either a kinematically hot bar (Pietrukowicz et al. 2012, 2015) or a pressure-supported spheroidal population (Dékány et al. 2013; Kunder et al. 2016; Prudil et al. 2019). The conflicting kinematic patterns between stars with different metallicities suggest that the Milky Way bulge/bar is a composite system

From a chemical standpoint, little agreement has been reached regarding the bulge/bar's true composition pattern. Early work indicated that inner bulge fields near Baade's Window are well described by closed box one-zone gas exhaustion models (e.g. Mat-

★ E-mail: chjohnson1@stsci.edu

teucci & Brocato 1990; Rich 1990). However, subsequent analyses that included outer bulge fields revealed the presence of a vertical metallicity gradient (Zoccali et al. 2008; Johnson et al. 2011, 2013a; Gonzalez et al. 2013), and many modern large sample surveys claim to find anywhere from 2 to 5 populations with distinct [Fe/H][1] values (e.g. Hill et al. 2011; Ness et al. 2013a; Bensby et al. 2017; Rojas-Arriagada et al. 2017; Zoccali et al. 2017; García Pérez et al. 2018; Duong et al. 2019). Although some 'peaks' in the bulge's metallicity distribution function may represent contributions from the halo and disc, the true nature of any metallicity gradient, the actual number of distinct components existing in the bulge, and whether a metallicity gradient extends into $|b| < 2^\circ$ (e.g. Rich, Origlia & Valenti 2012; Schultheis et al. 2015; Ryde et al. 2016; Schultheis et al. 2019) remain open questions.

Further issues regarding the formation, evolution, and structure of the bulge are raised when considering the detailed chemical abundances and age estimates. The inflection point in plots of [α/Fe] versus [Fe/H] for the metal-poor bulge ($-1 <$ [Fe/H] < 0) and thick disc is a particular area of contention. Some studies find that the bulge remains α-enhanced to a higher metallicity than the local thick disc, which would be consistent with a more rapid enrichment time-scale (e.g. Zoccali et al. 2006; Fulbright, McWilliam & Rich 2007; Johnson et al. 2011; Bensby et al. 2013; Johnson et al. 2014; Bensby et al. 2017; Rojas-Arriagada et al. 2017). However, others find that the bulge and local thick disc trends are identical (e.g. Meléndez et al. 2008; Alves-Brito et al. 2010; Gonzalez et al. 2011a; Jönsson et al. 2017; Zasowski et al. 2019). Similar disagreements are also found when considering the light and heavy elements (e.g. see reviews by Rich 2013; McWilliam 2016; Barbuy et al. 2018), and small composition differences may exist between the inner and outer bulge populations as well (e.g. Johnson et al. 2012).

Although bulge stars are overwhelmingly old with an age of $\sim$10 Gyr (e.g. Ortolani et al. 1995; Zoccali et al. 2003; Clarkson et al. 2008; Valenti et al. 2013; Renzini et al. 2018; Surot et al. 2019), microlensed dwarf analyses have suggested that a significant fraction of metal-rich bulge stars are <3–8 Gyr old (Bensby et al. 2011, 2013, 2017). Furthermore, Saha et al. (2019) claim to have found a conspicuous young ($\sim$1 Gyr) population of 'blue loop' stars in Baade's window. However, nearly all colour–magnitude diagram (CMD) investigations have ruled out a young bulge population that exceeds the few per cent level (Clarkson et al. 2008; Valenti et al. 2013; Renzini et al. 2018; Surot et al. 2019), and the bulge's RR Lyrae population may even contain some of the oldest known stars in the Galaxy (e.g. Savino et al. 2020). On the other hand, Ness et al. (2014b) suggest that young bulge stars may be tightly constrained near the plane, and Haywood et al. (2016) claim that young stars may be difficult to detect in typical CMDs due to degeneracy between age and metallicity. A clear solution to the bulge's age distribution problem is still lacking but will be required to fully understand its formation history.

The bulge's accretion history remains an important but unknown quantity as well, and may be closely connected to the existing observational evidence of a classical bulge component. For example, Pietrukowicz et al. (2015) discovered the existence of two distinct RR Lyrae populations in the bulge that exhibit separate sequences in period–amplitude diagrams, and Lee & Jang (2016) suggested that the two populations may be driven by He abundance differences following a pollution mechanism similar to those thought to occur in globular clusters. As a result, a significant portion of the Galactic bulge may have been accreted from disrupted 'building blocks', such as globular clusters. In fact, Ferraro et al. (2009, 2016) interpret the peculiar multiple populations in Terzan 5 as evidence that this cluster is a surviving example of a primordial bulge component.

Further examples of accretion include the presence of possible dwarf nuclei cores such as the globular clusters NGC 6273 (Johnson et al. 2015, 2017) and FSR 1758 (Barbá et al. 2019), double mode RR Lyrae with peculiar period ratios (Soszyński et al. 2014; Kunder et al. 2019), N-rich (Schiavon et al. 2017) and Na-rich (Lee et al. 2019) stars with potential cluster origins (but see also Bekki 2019), high velocity stars with retrograde orbits (e.g. Hansen et al. 2016), and the existence of at least one r-process enhanced star with a possible dwarf galaxy origin (Johnson, McWilliam & Rich 2013b). Many of these objects have been found in the outer bulge, which suggests that the inner and outer bulge may trace different formation and/or enrichment paths.

Several of the results described above were products of spectroscopic surveys such as the Bulge Radial Velocity Assay (Rich et al. 2007; Kunder et al. 2012), Abundances and Radial velocity Galactic Origins Survey (Freeman et al. 2013), GIRAFFE Inner Bulge Survey (GIBS; Zoccali et al. 2014), Gaia-ESO Survey (Gilmore et al. 2012), and Apache Point Observatory Galactic Evolution Experiment (APOGEE; Majewski et al. 2017) along with photometric surveys such as the Vista Variables in the Via Lactea (VVV; Minniti et al. 2010), Optical Gravitational Lensing Experiment (OGLE; Udalski, Szymański & Szymański 2015), and Two Micron All Sky Survey (2MASS; Skrutskie et al. 2006). Due to the large and variable extinction across most of the bulge, many of these surveys are optimized for near-infrared (IR) observations. However, deep optical and near-ultraviolet (UV) observations are still feasible along most bulge sightlines, and improved reddening maps (e.g. Gonzalez et al. 2013; Simion et al. 2017) from near-IR surveys make accurate, large-scale extinction corrections possible. The inclusion of optical, and particularly near-UV, photometry in the bulge significantly enhances the impact of previous surveys and permits detailed investigations into the bulge's metallicity distribution, structure, and UV-bright populations.

Given the paucity of uniform optical and near-UV photometry in the bulge, we present details regarding project performance, analysis methods, and early science results from the Blanco DECam Bulge Survey (BDBS). BDBS takes advantage of the Dark Energy Camera's 2.2 deg field of view (Flaugher et al. 2015) to survey >200 contiguous square degrees of the Southern Galactic bulge (see Fig. 1) in the *ugrizY* filters. BDBS extends to higher Galactic latitudes than the primarily optical DECam Plane Survey (DECaPS; Schlafly et al. 2018), and also reaches lower declinations than the Panoramic Survey Telescope and Rapid Response System (Pan-STARRS; Chambers et al. 2016) project. Critically, BDBS includes the *u* band, which we show to be an efficient metallicity discriminator for red clump giants.

2 OBSERVATIONS AND DATA REDUCTION

The data presented here were obtained using the wide-field DECam imager mounted on the Blanco 4-m Telescope at Cerro Tololo Inter-American Observatory during windows spanning 2013 June 1–5, 2013 July 14 and 15, and 2014 July 14–21. As illustrated in the *r*-band source density map of Fig. 1, the BDBS footprint provides nearly contiguous coverage from $l \sim -11^\circ$ to $+11^\circ$ and $b \sim -2^\circ$ to -9°, and extends down to $b \sim -13^\circ$ within 3° of the minor axis. Approximately, 90 unique DECam 'pointings' were required to

[1] $[A/B] \equiv \log(N_A/N_B)_{star} - \log(N_A/N_B)_\odot$ for elements A and B.

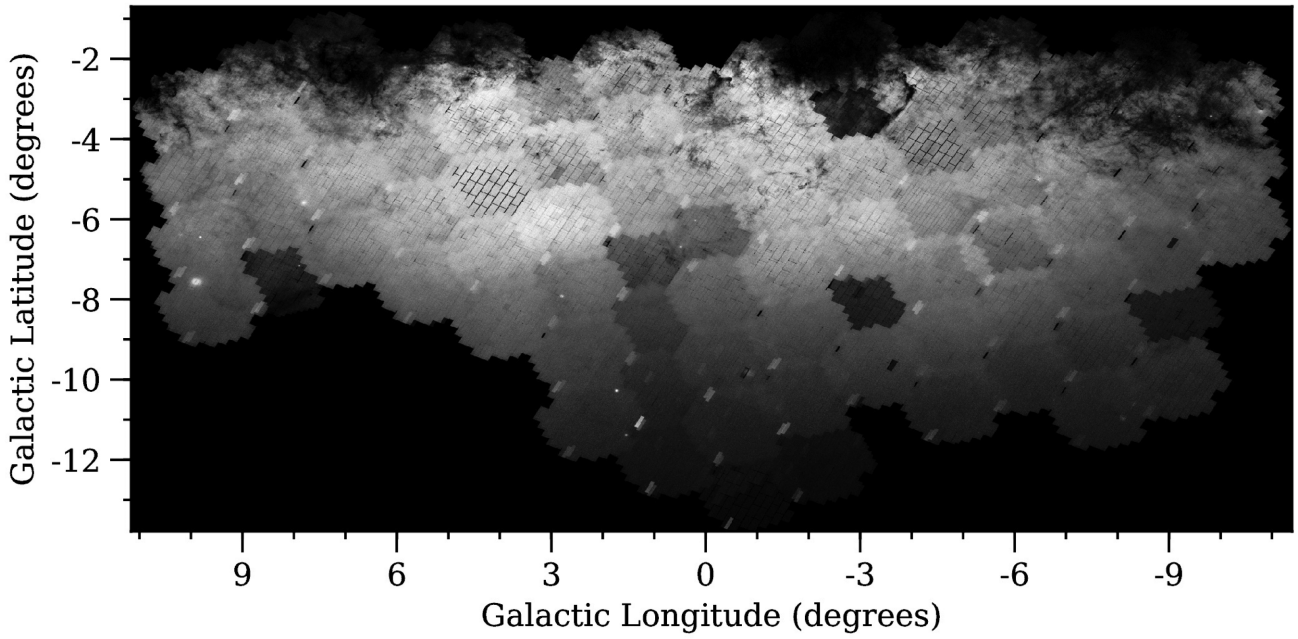

Figure 1. A binned source density map comprising 243 959 076 objects is shown for the contiguous BDBS footprint. Substantial extinction limits optical depth along lines of sight with $b \gtrsim -3°$, while incomplete observations and/or poor observing conditions resulted in fewer detections for a small number of fields (identified here by lower mean intensity levels). More than 25 globular clusters are visible, including notable objects such M 22 $(l, b) = (+9.89, -7.55)$ and FSR 1758 $(l, b) = (-10.78, -3.29)$. The DECam field of view is also visible for some fields where multiple dithers could not be obtained.

cover the desired sky area while also allowing for ∼10 per cent area overlap between adjacent fields.

For all filters, the 'long' exposures typically followed a four or five point dither pattern to fill in the substantial gaps between each of the 61 CCDs[2]; however, for the *r* band an additional, smaller five point dither pattern was used to ensure adequate sampling of the point spread function (PSF). These observations are intended to serve as a first epoch for future work aimed at obtaining DECam-only proper motions. 'Short' and 'ultrashort' exposures were also obtained in order to mitigate saturation issues with bright bulge red giant branch (RGB) stars, but these observations generally only followed a two-point dither pattern. For the *grizY* bands, the long, short, and ultrashort exposures were of order 75, 5, and 0.25 s, respectively. The long, short, and ultrashort exposure times for the *u* band were typically 150, 30, and 1.5 s, respectively. A sample DECam field of view for the *r* band, along with comparisons of the globular cluster NGC 6569 in long and ultrashort exposures, is provided in Fig. 2. Note that all observations were taken with 1 × 1 binning, which is equivalent to a plate scale of ∼0.263 arcsec pixel^{-1} (Flaugher et al. 2015).

The sky conditions were generally photometric for the 2013 runs, but the seeing and cloud cover were highly variable during the 2014 run.[3] The seeing, based on the measured FWHM (full width at half-maximum) of all *r*-band images, ranged from ∼0.8 to 1.8 arcsec, with an average of 1.1 arcsec ($\sigma \sim 0.2$ arcsec). The poor sky conditions in 2014 primarily affected the short and ultrashort exposures, which were a priority in the last run, but also limited the observing depth

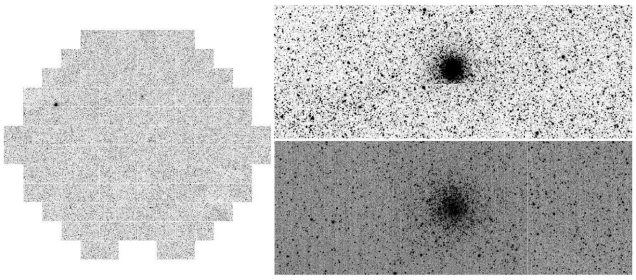

Figure 2. Left: a sample 75 s DECam *r*-band exposure of a field near $(l, b) \approx (-0.21, -6.29)$, which includes the globular clusters NGC 6569 (left) and NGC 6558 (middle), is shown. Approximately 1.9 × 10^6 sources were detected in this image. Right: a zoom-in of the region near NGC 6569 is shown for a 'long' (75 s; top) and 'ultrashort' (0.25 s; bottom) *r*-band exposure. North is up and East is to the left for all panels.

in some fields. An example of the depth limitations can be seen in the $(l, b) = (-3, -8)$ field of Fig. 1, which has a much lower source density than surrounding fields. The field of view was also reduced to 60 CCDs, instead of the nominal 61, for the 2014 run, which further affected the observational efficiency. Nevertheless, Fig. 3 shows that a majority of the fields reached approximately the same depth in each filter, for a single long exposure. Median calibrated 5σ image depths for the *ugrizy*[4] bands are approximately 23.5, 23.8, 23.5, 23.1, 22.5, and 21.8 mag, respectively. Additional information regarding observing strategies, calibration fields (Sloan Digital Sky Survey, SDSS equatorial Stripe 82 with right ascensions of 10, 12, and 14 h), and a catalogue of observation dates for each field is provided in Rich et al. (2020, submitted).

[2]DECam nominally has 62 CCDs but detector N30 is not used due to an overillumination event that occurred in 2012 November (see http://www.ctio.noao.edu/noao/content/Status-DECam-CCDs).

[3]Time-lapse video from the radiometric all-sky infrared camera (Lewis, Rogers & Schindler 2010) are available on Youtube for each night.

[4]Note that the *y*-band magnitudes listed in Fig. 3 were calculated after the DECam *Y* magnitudes were converted on to the $y_{\rm ps1}$ system.

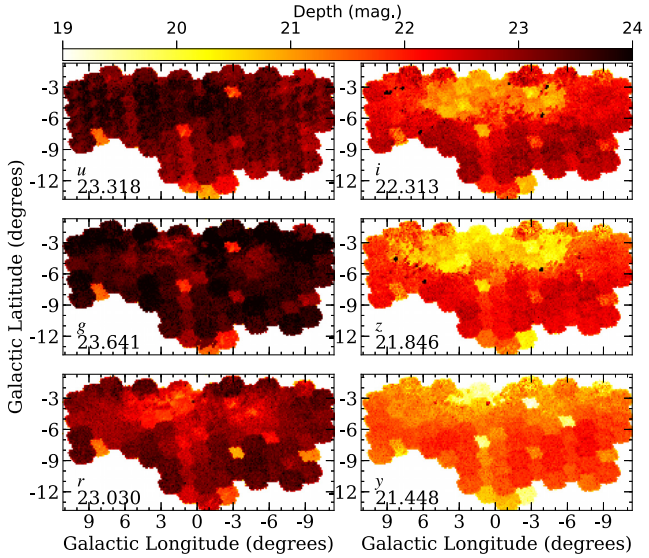

Figure 3. Field depths are shown as a function of both filter and sky position. The colour gradient in each bin represents the *ugrizy* magnitude of the faintest star with a S/N ratio of at least 5. Median image depths are provided in each panel.

All raw data products were processed using the NOAO Community Pipeline (Valdes et al. 2014), which automatically performs calibrations for issues such as: overscan and bias correction, cross-talk, flat-fielding, fringe removal, pupil correction, and World Coordinate System (WCS) mapping. Both the raw and pipeline reduced images are available for download on the NOAO Science Archive.[5] We note that all of the data presented here are based on analyses of the calibrated images, and we did not incorporate the weight maps, data-quality masks, or other Community Pipeline data products.

3 DATA ANALYSIS AND BDBS PIPELINE DESCRIPTION

3.1 Data management

The data volume for all Community Pipeline processed BDBS science and calibration fields totaled ∼15 terabytes (TB) of space when uncompressed. The number of utilized DECam images, which were obtained under acceptable but not necessarily photometric conditions and for which a successful WCS was found, totalled ∼7600, and is equivalent to >450 000 unique CCD images. Given the large data volume and millions of files required to organize and analyse the DECam images, we stored and processed all BDBS data on Indiana University's (IU) 5 petabyte (PB) Data Capacitor II high speed shared storage system, which is managed by the Pervasive Technology Institute (PTI). The IU system provided a central interface for the core BDBS investigators, which were spread across various institutions, to process and share data products.

Fig. 4 provides a basic outline of the data flow, file management, and processing scheme used for BDBS. Briefly, the Community Pipeline calibrated images were transferred from the NOAO Science Archive to the IU system via the parallel file transfer protocol tool provided by NOAO. At the highest level, images were partitioned into directories based on image type (calibration or science). Calibration frames were further separated based first on the night of observation and then by filter. Similarly, science frames were organized first by field centre and then by filter. For reference, Fig. 5 shows the mean central position on the sky of each CCD within a given pointing 'block'.

The multilevel data organization scheme has several practical and computational advantages. For example, generating multiple directories based on image metadata reduces the number of files within a subdirectory to a manageable level and speeds up operating system calls, such as file queries. Additionally, an intuitive but descriptive file system structure provides a simple means for fast data archiving and compression, which is necessary for both long- and short-term storages.

Critical BDBS files that are not archived by NOAO, such as intermediate pipeline files, software products, and final catalogues, were placed into long-term storage on IU's 79 PB Scholarly Data Archive. All data products were temporarily stored on IU's Data Capacitor system for ∼1 yr and accessed via the Karst high-throughput computing cluster. The final catalogue release paper will describe additional long-term storage and access solutions.

3.2 Photometry pipeline

In order to take advantage of the distributed processing power of the IU supercomputing system, the mosaic DECam images mentioned in Section 3.1 were separated into individual CCD frames before entering the BDBS photometry pipeline. As illustrated in Fig. 4, all of the photometric measurements were obtained using the PSF fitting DAOPHOT/ALLSTAR crowded field photometry software suite (Stetson 1987), as distributed by the Starlink Project[6] (Currie et al. 2014). The DAOPHOT/ALLSTAR interface was automated using a wrapper written in FORTRAN 2008 that handled all of the input/output (I/O) commands. DAOPHOT/ALLSTAR was used to perform actions such as: finding stars in an image, identifying acceptable bright PSF stars (>100 per image for science fields; >10 per image for Stripe 82 calibration fields), fitting a quadratically varying Gaussian PSF for each 2K × 4K CCD, fitting and subtracting PSF models of stellar objects, and performing aperture photometry on images where all objects except the PSF stars have been subtracted (for growth-curve analyses). The general analysis procedure followed the recipe outlined in Stetson (1987),[7] and involved three 'fit and subtract' passes with DAOPHOT/ALLSTAR. A final step in the pipeline converted the centroid *X*,*Y* pixel coordinates into right ascension and declination coordinates using the 'xy2sky' subroutine from WCSTOOLS (Mink 2002), which further utilized the WCS from the image headers.

3.2.1 *Photometry pipeline implementation*

The CCD images were processed through the BDBS pipeline on one of IU's high-performance shared storage systems. Since the FORTRAN wrapper was designed to run DAOPHOT/ALLSTAR independently on a single CCD image, a PYTHON job generator script was constructed to scan all image folders and publish a job message to an Advanced Message Queuing Protocol (AMQP) queue system. The AMQP

[5]The NOAO Science Archive can be accessed at: http://archive1.dm.noao.edu/.

[6]The Starlink software is currently supported by the East Asian Observatory and can be accessed at: http://starlink.eao.hawaii.edu/starlink.

[7]See also http://www.star.bris.ac.uk/∼mbt/daophot/mud9.ps.

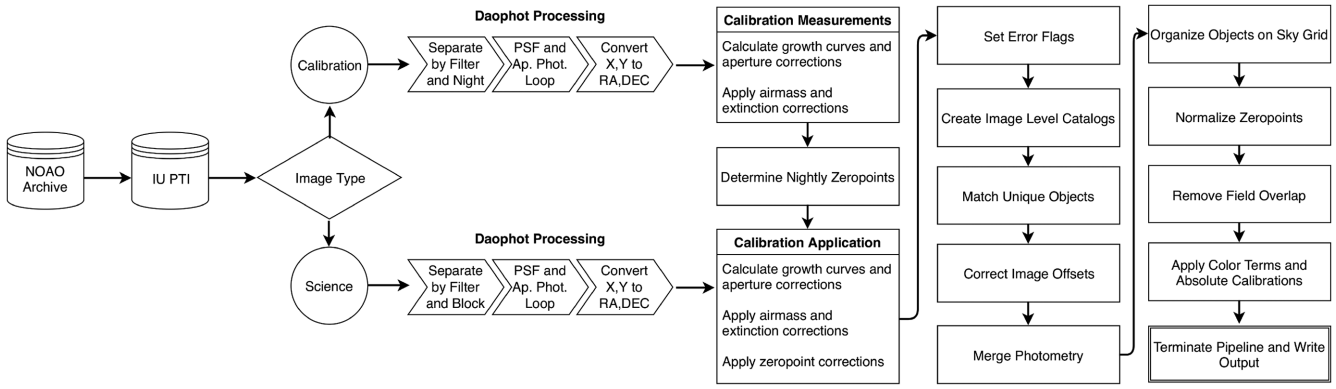

Figure 4. A schematic diagram illustrating the data organization, data flow, and general pipeline procedures. Note that the final *u*-band calibration was determined using DECam observations of the SDSS (Alam et al. 2015) Stripe 82 field, but *g*, *r*, *i*, *z*, and *y* were calibrated using direct overlap with the Pan-STARRS survey (Chambers et al. 2016).

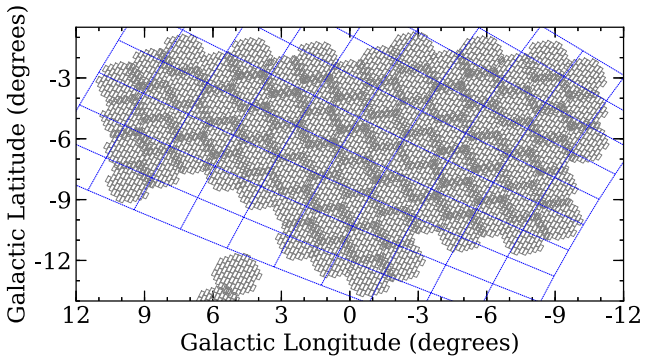

Figure 5. The sky positions of individual CCD images are illustrated for the BDBS footprint with solid grey lines. Each set of 60–61 CCDs represents a unique pointing that included 2–15 additional small dithers for each band (not shown). The data were organized and photometered separately by pointing and band, and were later organized on to the fixed sky grid shown by the blue dashed lines. The sky grid follows lines of constant right ascension and declination. Note that a few additional fields, such as the Sagittarius dwarf spheroidal galaxy, were also observed for BDBS but are omitted because they do not directly overlap with the contiguous portion of the survey. We anticipate including the Sagittarius dwarf photometry in the final data release.

job messages were shuffled so that the images were processed non-sequentially. As mentioned previously, a major advantage of this method is that different computing nodes were not simultaneously competing for access to the same folder on the shared storage system, which would otherwise be a time consuming I/O bottleneck. Similarly, since the pipeline required certain static files in order to run (e.g. daophot.opt; allstar.opt; etc.), we avoided name conflicts by processing all CCD frames in separate temporary subdirectories.

A set of 10 nodes, each with two 12-core Intel Xeon E5-2680 v3 processors, were reserved on the Carbonate computing cluster at IU for the maximum allowable wall-time of 14 d. On each node eight instances of a PYTHON script were initiated that retrieved a job message from the aforementioned queue, executed the FORTRAN-based BDBS pipeline on a single CCD frame, logged usage statistics, and then drew another job message from the queue. Additional nodes were acquired when the initial allocation was consumed. For the final production run, the BDBS pipeline required ∼3 weeks of wall-time and utilized a total of ∼2.2 yr of processor time on IU's Carbonate cluster. Approximately 10^{10} objects were identified when including all images and filters.

3.2.2 *Aperture and nightly zero-point corrections*

At this point in the pipeline, the calibration and science fields contain an output file for each successfully run CCD frame that included metadata from the analysis (e.g. FWHM; exposure time; filter and CCD ID; etc.) and for each star the measured RA/Dec. coordinates, X/Y pixel positions, instrumental magnitude, standard magnitude error, local sky brightness estimate, and the 'chi' and 'sharpness' parameters produced by DAOPHOT/ALLSTAR. As mentioned previously, separate aperture photometry files are also included for all stars in the calibration frames but only the PSF stars in the science frames.

For each unique combination of observation night and filter, the aperture photometry files for both the science and calibration fields were copied into temporary directories and processed with an implementation of the 'DAOGROW' growth-curve algorithm described in Stetson (1990). This procedure produced a mean aperture correction for each image that was applied to convert the relative PSF magnitudes on to an absolute zero-point scale. Typical aperture corrections were of order −0.3 mag.

Atmospheric extinction corrections were applied to all calibration and science instrumental magnitudes using the airmass values provided in the image headers and the extinction coefficients provided by NOAO.[8] For the *ugriz* filters, the Stripe 82 instrumental magnitudes were matched to the calibrated AB photometry from SDSS (Alam et al. 2015), while the *Y*-band data were matched to the UKIRT Infrared Deep Sky Survey Large Area Survey (UKIDSS-LAS; Lawrence et al. 2007). Note that the UKIDSS-LAS *Y*-band data were converted from $Y_{\rm VEGA}$ to $Y_{\rm AB}$ using the relation,

$$Y_{\rm AB} = Y_{\rm VEGA} + 0.634, \quad (1)$$

from Hewett et al. (2006).

Mean zero-point values were iteratively calculated for each night and filter using the Stripe 82 calibration frames, and were applied to the appropriate aperture corrected science frame magnitudes. Fig. 6

[8]Estimates for photometric zero-points, colour corrections, and extinction corrections are provided at: http://www.ctio.noao.edu/noao/content/Mean-Photometric-Standard-Star-Module-PSM-Solutions-mean-zeropoints-colour-terms-extinctions.

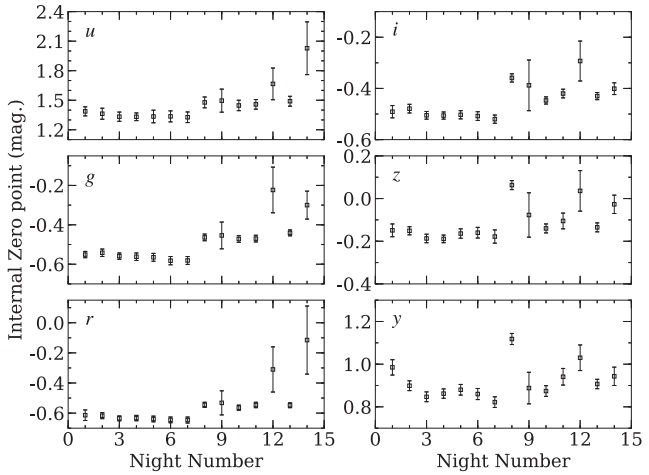

Figure 6. The median internal zero-point values, calculated using all CCDs and exposures, are shown as open boxes for each filter of each observing night. The error bars represent the median absolute deviations and are based on sample sizes of ∼10 000 stars in the Stripe 82 fields. Nights 1–5, 6–7, and 8–14 span 2013 June and July, and 2014 June, respectively. Typical median absolute deviation values are of order ∼0.02 mag., but during the worst observing conditions the scatter reaches ∼0.1 mag.

illustrates the median internal zero-point values for each observing night and filter, and clearly indicates that the 2013 observation conditions were superior to those of 2014. The application of these internal zero-point corrections provided a blunt tool to correct for the different observing conditions on a night-to-night basis.[9]

3.3 Catalogue generation and final calibration

3.3.1 Initial catalogues

Before merging the individual CCD results into image level catalogues (i.e. all 60–61 CCDs from a single DECam exposure), the pipeline automatically determined simple quality control metrics based on a star's photometric measurement error, local sky estimate, and chi value relative to other objects within a 0.05 mag wide bin on the same chip in the same exposure. For bins where the number of objects was <100 (e.g. bright stars), the bin sizes were increased until 100 targets were included. Quality flags were set to indicate the number of standard deviations away from the mean that each detection's error, sky, and chi values resided. Additional flags were added to the CCD level catalogues to further indicate whether an exposure was long (>30 s) or short (≤30 s) and whether it was obtained during a photometric or non-photometric night, as assessed from Fig. 6.

For each exposure of each filter within a given pointing block (e.g. see Fig. 5), the CCD level catalogues were collated into image level catalogues (i.e. all 60–61 CCD files of a single image were merged) in order to: identify unique detections, measure and correct residual image-to-image zero-point offsets, and generate a data base of photometry measurements for each unique source. Before processing, the image level catalogues were indexed by sorting via right ascension. The coordinate sorting was accomplished by modifying a standard FORTRAN 2008 heapsort algorithm to operate on multidimensional arrays of varying data types, rather than just a 1D floating point array.

The adopted coordinate indexing scheme permitted the use of a bisecting ordered search algorithm, which can quickly ($O \sim \log_2 N$) find upper/lower index boundaries in a 1D array when given minimum and maximum values. We utilized this code to first produce a list of unique detections within each pointing block and for each filter. To generate the unique source list, a boolean array was constructed to flag whether an object had been previously matched to any other detection in the master list, for a given filter. If a target of interest had not yet been discovered then the pipeline would scan the master catalogue and perform a coordinate search with a radius of 1 arcsec. The bounding box for the coordinate search was analytically calculated with:

$$\delta_{\rm min.} = \delta_{\rm o} - r, \tag{2}$$

$$\delta_{\rm max.} = \delta_{\rm o} + r, \tag{3}$$

$$\alpha_{\rm min.} = \alpha_{\rm o} - \arcsin(\sin(r)/\cos(\delta_{\rm min.})), \tag{4}$$

$$\alpha_{\rm max.} = \alpha_{\rm o} + \arcsin(\sin(r)/\cos(\delta_{\rm max.})), \tag{5}$$

where r is the search distance, $\alpha_{\rm o}$ and $\delta_{\rm o}$ are the central right ascension and declination, and $\alpha_{\rm min.}$, $\alpha_{\rm max.}$, $\delta_{\rm min.}$, and $\delta_{\rm max.}$ are the minimum and maximum right ascensions and declinations of the bounding boxes. All objects inside the 1 arcsec search radius were flagged as matches to avoid double counting and unnecessary future searches, but only the closest match was registered. The catalogue index values for all matches of unique objects were saved in a 2D matrix for rapid retrieval. Coordinate statistics, such as median values, dispersions, and covariances, were calculated for each unique object.

3.3.2 Intermediate catalogues

Separate intermediate catalogues were produced for each filter, and included the internal photometric measurements and associated metadata for every unique detection in a given band. Since the observations are spread over two years and variable sky conditions, these intermediate catalogues were used to calculate residual median zero-point offsets between image pairs using well-measured bright (14–18 mag) stars. For each filter and sky block combination, a reference image was chosen to serve as the zero-point anchor. Priority for the reference images was given first to long and then short exposures taken on photometric nights, primarily in 2013 (see Fig. 6), long and then short exposures taken on partially photometric nights, and then long or short exposures taken on non-photometric nights. Each intermediate catalogue maintained a flag to indicate the type of reference image used.

The procedure described above ensured that for a given band all photometric measurements shared a common, but not necessarily accurate, zero-point. Therefore, all photometric measurements for each unique object in each filter could be combined to reduce the observed scatter. For objects with five or more measurements in a given filter, a simple sigma clipping algorithm was utilized to remove

[9]One amplifier of the S7 CCD is unstable and has poor linearity (see http://www.ctio.noao.edu/noao/node/2630), but as noted in Schlafly et al. (2018) the CCD nominally performs well. Therefore, we did not discard photometry from this CCD and treated the problematic amplifier the same as all the others. Erroneous photometry from this amplifier should be removed during the catalogue merging process, but may persist in cases where only one observation of a star on that amplifier was available.

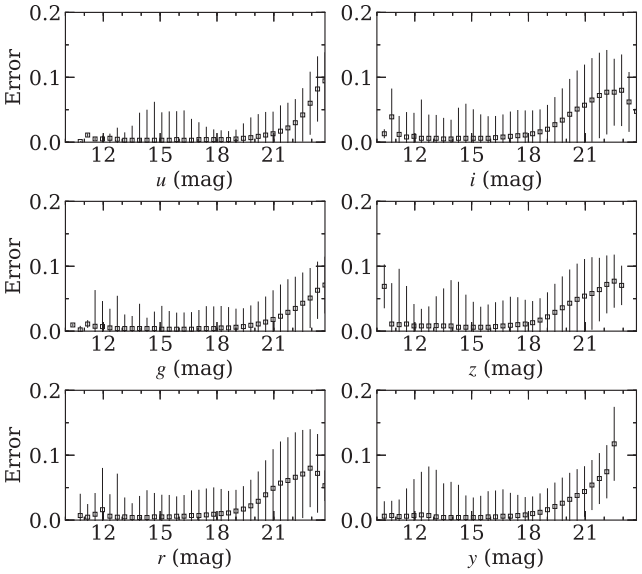

Figure 7. Binned median photometric errors are shown for the *ugrizy* bands analysed for BDBS. The data are from a roughly 2 sq deg field centred near $(l, b) = (0°, -6°)$ and represents a typical BDBS pointing. The error bars trace the median absolute deviations within each bin. Note that the panels only include targets for which at least two clear detections were present in a given band. However, the total number of observations can range from 2 to more than 15 for a given object.

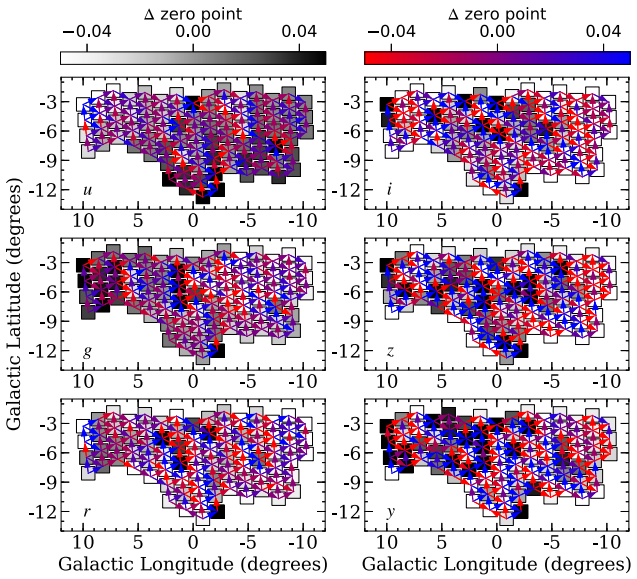

Figure 8. Each box represents a unique pointing 'block' (e.g. see Fig. 5) with the filled grey scale colours representing the subtracted zero-point corrections from the singular value decomposition. The field-to-field zero-point offsets range from −0.05 mag (white) to +0.05 mag (black). Since only a small number of fields in each filter had absolute corrections > 0.05 mag, the colour gradient was saturated at ±0.05 mag. The red (−0.05 mag) to blue (+0.05 mag) lines indicate the sign and magnitude of the offsets between individual fields. The arrows illustrate the direction in which the zero-point offsets were calculated.

extreme outliers before combining.[10] However, objects with four or fewer measurements included all values in the weighted average. A weight array was determined for each photometric value using the inverse of the measurement variance. A weighted measurement uncertainty was also determined along with a naive unweighted error value representing the uncertainty values from each image added in quadrature. A summary of the weighted error distribution as a function of magnitude for all filters, but only including objects for which two or more detections were present, is provided in Fig. 7. The numerical error flags described in Section 3.3.1 were also combined using the same weight array to produce a simple measurement quality flag. The number of combined measurements for each star was recorded and ranged from one to more than 15 for >400 million detections.

3.3.3 Final catalogues

The intermediate cataloguing phase identified unique objects within a dithered pointing block, corrected the instrumental magnitudes for atmospheric extinction, applied a rough but uniform zero-point correction to the AB system (Oke & Gunn 1983), and calculated a weighted average magnitude for each object. However, Fig. 5 shows that significant overlap exists between pointing blocks, which means that some stars are present in more than one intermediate catalogue. Furthermore, most intermediate catalogue zero-points were anchored to a long exposure data set taken on a photometric night, but some were only anchored to long/short exposures taken on partially or non-photometric nights.

Since not all objects are detected in every filter, we selected the *r* band as a compromise astrometric filter (i.e. the final coordinates are based on the WCS from *r*-band images only and an object is only in the final catalogue if it has at least one clear *r*-band measurement).[11] For each pointing block, the unique object lists for each passband were filtered against the *r*-band source list using the same sort/search algorithms described in Section 3.3.1.

Before merging the photometry for detections that appear in two or more fields, we used these objects to calculate the residual field-to-field zero-point differences between adjacent fields. The results of this process are illustrated by the coloured arrows shown in Fig. 8, and largely reflect differences in observing conditions between the reference frames described in Section 3.3.2. Median field-to-field offsets and absolute deviations for the *ugrizY* filters were −0.002 (0.019), −0.003 (0.019), −0.002 (0.026), −0.005 (0.035), −0.005 (0.064), and −0.003 (0.078) mag, respectively, and were based on an average of 2000 (*u*) to 80000 (*Y*) bright stars per field.

Fig. 8 shows that all fields contain at least two adjacent neighbours with object overlap and therefore a simple field-to-field offset correction is not practical. Instead, we selected a pointing block where all observations in all filters were obtained on the same photometric night in 2013 to serve as a reference field. A global solution for the field-to-field offsets in each filter that minimizes the zero-point differences between all fields was then obtained via singular value decomposition. The resulting zero-point shifts applied to each field are illustrated by the filled boxes in Fig. 8. Median absolute deviations for the applied offsets in the *ugrizY* filters were 0.020, 0.022, 0.018, 0.040, 0.036, and 0.046 mag, respectively.

With the entire data set now placed on a consistent zero-point scale that is ultimately tied to an exposure set obtained on a photometric

[10]Note that our adopted measurement combination method is biased against variable sources. Objects with magnitudes that vary significantly over the course of hours to days, such as RR Lyrae, are under-represented in our final catalogues.

[11]Since the *r*-band colour correction also requires a *g*-band measurement, technically a star will only appear in the final catalogue if it has photometry from both *g* and *r*.

night, objects within each pointing block were allocated into the appropriate absolute sky grid bins illustrated in Fig. 5. A final sort and search pass was performed within each sky grid to match repeat observations (i.e. objects that appeared in two or more pointing blocks) and merge their photometry using the weighted averaging scheme described in Section 3.3.2. This procedure produced a set of 77 catalogues where all photometry for a unique object has been merged and repeat observations have been excised.

3.3.4 Absolute calibration

To complete the catalogue collation process, colour transformations and absolute zero-point corrections were applied to the entire data set. Although BDBS aims to calibrate on to the AB system, no single reference data set is available that runs from the near-UV to near-IR. For example, SDSS only includes *ugriz* whereas Pan-STARRS only has *grizy*. Since a significant fraction of the BDBS footprint, along with most of the utilized filters, overlays with Pan-STARRS, we calibrated the BDBS data on to the Pan-STARRS *grizy* system and reserved the Stripe 82 SDSS calibration only for the *u* band.

The *u*-band calibration was relatively straightforward and utilized the Stripe 82 observations from the same photometric night as the internal zero-point frame described in Section 3.3.3. The *u*-band calibration from the internal BDBS system to SDSS utilized the $u - g$ colour term, which also required the $g - r$ term, and was calculated using:

$$g_{\rm BDBS} = g_{\rm int.} - [-0.109(g-r)_{\rm SDSS} + 0.056], \quad (6)$$

$$r_{\rm BDBS} = r_{\rm int.} - [-0.079(g-r)_{\rm SDSS} + 0.042], \quad (7)$$

$$u_{\rm BDBS} = u_{\rm int.} - [0.008(u-g)_{\rm SDSS} - 0.010], \quad (8)$$

where $u_{\rm BDBS}$ represents the calibrated *u*-band magnitude in the final BDBS catalogue, $u_{\rm int.}$ is the internal uncalibrated magnitude, and $(u - g)_{\rm SDSS}$ is the iteratively determined $u - g$ colour corrected to the SDSS system. Note that equation 8 is relevant for stars with $0.75 \lesssim (u - g)_{\rm SDSS} \lesssim 2.75$ mag. Residuals between the final calibrated $u_{\rm BDBS}$ magnitudes and those in the SDSS catalogue for the Stripe 82 calibration field are shown in Fig. 9. The median absolute deviation for stars with magnitudes between 15 and 19 is 0.032 mag. Similar comparisons are also provided in Fig. 9 for the *g* and *r* filters. Since the *u*-band data are calibrated using the SDSS data from Alam et al. (2015), an equivalent shift of 0.02 mag may need to be added to the BDBS *u*-band data to place it on the formal AB system.[12]

As mentioned previously, the *grizy* filters were calibrated directly using overlap between Pan-STARRS and BDBS. In particular, we selected the zero-point reference field from Section 3.3.3 and three adjacent fields that were also observed on completely photometric nights as the calibration sets. Since only the *g* and *r* filters are guaranteed to exist for all stars in the final catalogue, we utilized $g - r$ as the reference colour for the transformations between the internal BDBS *grizY* and Pan-STARRS *grizy* systems. By comparing bright (<18 mag) overlapping BDBS and Pan-STARRS detections in four reference fields, we determined the following transformation equations:

$$g_{\rm BDBS} = g_{\rm int.} - [-0.055(g-r)_{\rm PS1} - 0.039], \quad (9)$$

$$r_{\rm BDBS} = r_{\rm int.} - [-0.095(g-r)_{\rm PS1} - 0.042], \quad (10)$$

[12]For further information, we refer the interested reader to http://classic.sdss.org/dr7/algorithms/fluxcal.html.

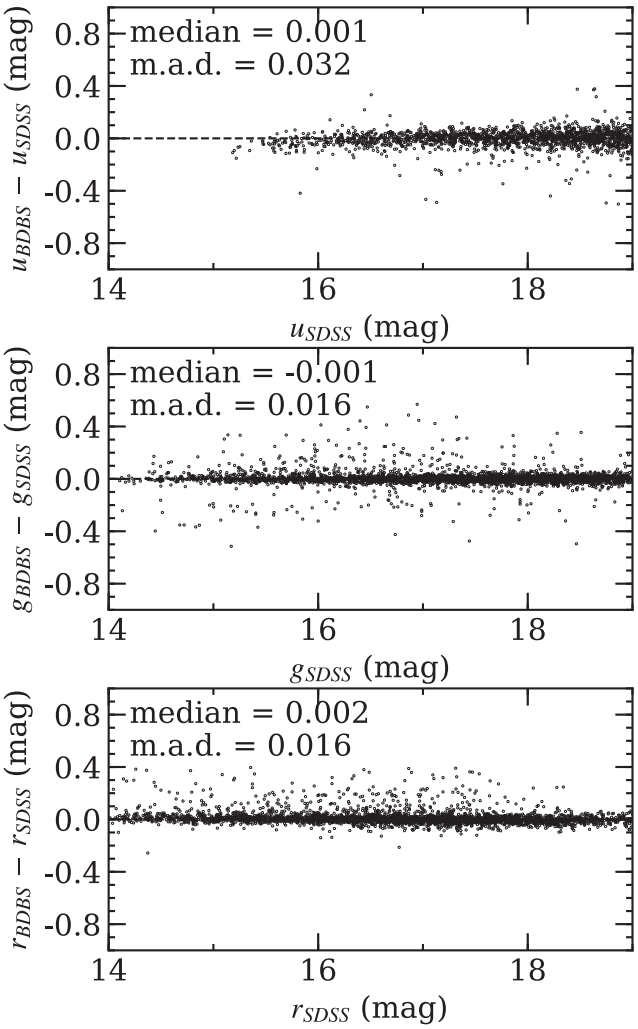

Figure 9. The top panel shows the difference between the $u_{\rm BDBS}$ and $u_{\rm SDSS}$ magnitudes as a function of $u_{\rm SDSS}$ for stars in the Stripe 82 calibration field. The Stripe 82 BDBS data were processed using the same code and settings as the science fields (see Fig. 4). Since the conversion from the internal magnitude system to the SDSS system included a colour term based on $u - g$, which also depends on $g - r$, similar comparisons are shown in the middle and bottom panel for the *g* and *r* bands. Note that the calibration equations used to transform the internal *g* and *r* magnitudes on to the SDSS system were only used for the purposes of the *u*-band calibration. The final *g* and *r* magnitudes were calibrated on to the Pan-STARRS system instead. The median magnitude differences and median absolute deviations (m.a.d.) are provided in all three panels.

$$i_{\rm BDBS} = i_{\rm int.} - [-0.079(g-r)_{\rm PS1} - 0.106], \quad (11)$$

$$z_{\rm BDBS} = z_{\rm int.} - [-0.087(g-r)_{\rm PS1} - 0.124], \quad (12)$$

$$y_{\rm BDBS} = Y_{\rm int.} - [-0.050(g-r)_{\rm PS1} - 0.082], \quad (13)$$

where similar to equation (8), the left-hand side of equations (9)–(13) represent the final BDBS magnitudes calibrated on to the Pan-STARRS system and the right-hand side of equations (9)–(13) include the internal uncalibrated magnitudes and the calibrated $(g - r)_{\rm PS1}$ colours. The calibrations above are relevant for stars with $(g - r)_{\rm PS1}$ colours between about −0.1 and 2.0 mag. As noted in Schlafly et al. (2018), additional offsets of order 0.020, 0.033, 0.024, 0.028,

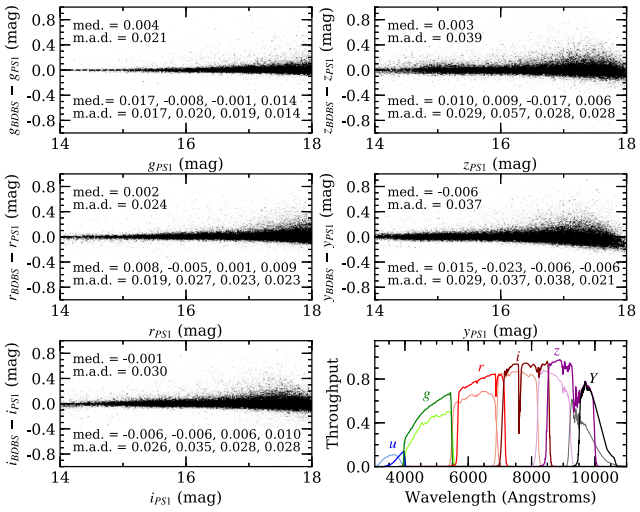

Figure 10. Similar to Fig. 9, photometric differences between BDBS and Pan-STARRS are plotted as a function of Pan-STARRS magnitudes for the *grizy* bands. The panels include four fields located at (l, b) $\approx$ (+3.5, −6.5), (+6.0, −5.5), (+7.0, −4.5), and (+9.0, −3.5), which were used for determining the calibration equations between the internal BDBS system and Pan-STARRS. The top median and median absolute deviation values include all four fields and the bottom sets indicate the statistics for individual fields. The bottom right panel shows throughput curves for the DECam u (blue), g (green), r (red), i (maroon), z (dark magenta), and Y (black) filters in comparison with the $u_{\rm SDSS}$ and $grizy_{\rm PS1}$ filters, which are shown as lighter colours.

and 0.011 may need to be added to the calibrated BDBS magnitudes to place them on the absolute AB scale.

A summary of the residuals between the calibrated BDBS magnitudes and the Pan-STARRS catalogue for overlapping objects in all four calibration fields is provided in Fig. 10. Note that a comparison between the filter transmission curves of DECam and SDSS/Pan-STARRS is provided in Fig. 10 as well. The individual median offsets for each of the four fields, along with the median absolute deviations, is also provided. The overall median absolute deviations for the *grizy* filters are 0.021, 0.024, 0.030, 0.039, and 0.037, respectively, and the field-to-field absolute calibration variance is generally $\lesssim$ 0.01–0.02 mag. We adopt the overall median absolute deviations from Fig. 10 as an estimate for the calibration uncertainty for the *grizy* filters. The final, calibrated BDBS catalogue contains 243 959 076 unique objects and will be released in a future publication.

3.4 Reddening and extinction corrections

Fig. 1 clearly shows that many BDBS lines of sight suffer from significant small- and large-scale differential extinction due to foreground dust. Therefore, we corrected for reddening using the high sampling (1 arcmin × 1 arcmin) extinction map from Simion et al. (2017), which covers most of the BDBS footprint ($|l| < 10^\circ$; $-10^\circ < b < +5^\circ$). The Simion et al. (2017) map was built using red clump giants from the VVV survey following the methods described in Gonzalez et al. (2011b, 2012), which provided the first VVV extinction maps but at a coarser (2 arcmin × 2 arcmin to 6 arcmin × 6 arcmin) spatial resolution.

Since the Simion et al. (2017) map is derived from the Visible and Infrared Survey Telescope for Astronomy (VISTA) photometric system, several transformations were required to obtain *ugrizy* extinction corrections. The VISTA $JK_{\rm S}$ photometry was first converted to the 2MASS system using equations (C4) and (C6) from González-Fernández et al. (2018),[13] and the reddening values were converted using the relation:

$$E(J-K)_{\rm 2MASS} = 1.081 E(J-K)_{\rm VISTA}. \quad (14)$$

These transformations were then combined with table 1 of Green et al. (2018) to determine $E(B-V)$ as:

$$E(B-V) = 2.045 E(J-K)_{\rm 2MASS}. \quad (15)$$

Finally, the extinction values for each filter were computed as:

$$A_{\rm u} = 4.239 E(B-V), \quad (16)$$

$$A_{\rm g} = 3.384 E(B-V), \quad (17)$$

$$A_{\rm r} = 2.483 E(B-V), \quad (18)$$

$$A_{\rm i} = 1.838 E(B-V), \quad (19)$$

$$A_{\rm z} = 1.414 E(B-V), \quad (20)$$

$$A_{\rm y} = 1.126 E(B-V), \quad (21)$$

using table 6 in Schlafly & Finkbeiner (2011) for the u band and table 1 of Green et al. (2018) for the *grizy* bands.

For the *grizy* bands, the adopted Green et al. (2018) extinction vector was based on a combination of broad-band stellar colours and APOGEE spectra (see also Schlafly et al. 2016). Since a majority of the APOGEE reference stars used to define the extinction vector reside within the disc and bulge, the adopted vector is appropriate to use for BDBS. For the u band, the Schlafly & Finkbeiner (2011) extinction vector was obtained by comparing the colours of synthetic spectra built using stellar parameters from the SEGUE Stellar Parameter Pipeline (Lee et al. 2008). By construction, the extinction vector for the u band is more appropriate for higher Galactic latitudes. However, in the absence of a more recent determination in high extinction regions we use the u-band extinction law for $R_{\rm V} = 3.1$ in table 6 of Schlafly & Finkbeiner (2011). We caution that a small error in the reddening law, or a small variation in the reddening law between different lines of sight, will produce large errors in the u-band extinction correction.

Extinction maps for the u and i bands, along with a sample $E(u-i)$ reddening map, are provided in Fig. 11. Note that the extinction and reddening maps from Simion et al. (2017) are only valid for BDBS stars with $|l| < 10^\circ$ and $b > -10^\circ$. Reddening corrections are not available at this time for fields with higher longitudes and/or latitudes. Additionally, a recent analysis by Hajdu et al. (2019) showed that spatially varying zero-point offsets of order 0.05–0.1 mag. in $E(J-K_s)$ are present in the VVV data. However, the largest zero-point deviations are limited to fields within ∼2° of the plane, where BDBS observations are sparse, and Simion et al. (2017, see their section 2) already corrected the VVV photometry for many of the effects noted in Hajdu et al. (2019).

[13] Additional information is provided by the Cambridge Astronomy Survey Unit at: http://casu.ast.cam.ac.uk/surveys-projects/vista/technical/photometric-properties. Note that we utilized version 1.3 of the VISTA data.

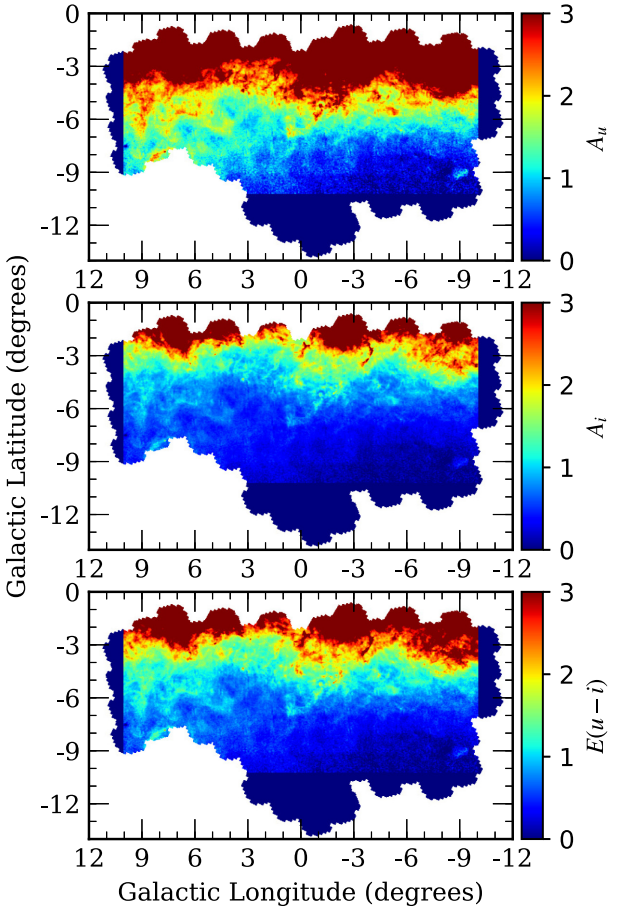

Figure 11. The top, middle, and bottom panels illustrate sample A_u, A_i, and $E(u - i)$ extinction and reddening maps used for BDBS. Equivalent maps exist for the *grzy* filters as well. The extinction and reddening values are based on the bulge maps presented in Simion et al. (2017). Note that the extinction and reddening values are only valid for fields with $|l| < 10°$ and $b > -10°$.

4 DATA VALIDATION AND EARLY SCIENCE RESULTS

4.1 A comparison with DECaPS and Pan-STARRS

As noted in Introduction, several recent surveys have employed large format imagers to observe low latitude disc and bulge fields in optical band passes. However, few of these surveys specifically aim to understand the formation history and structure of the Galactic bulge. For example, Pan-STARRS is geared toward obtaining uniform *grizy* photometry for all regions of the sky with $\delta \gtrsim -30°$. On the other hand, the DECaPS and VST Photometric Hα Survey (VPHAS+; Drew et al. 2014) programs use various combinations of the *grizy* (DECaPS) and *ugriH*α (VPHAS+) filters to primarily understand the Galactic disc. Saha et al. (2019) also used the *ugriz* filters on DECam to explore the Galactic bulge, but this work emphasizes RR Lyrae and focuses on a small number of fields that span ∼1 per cent of the BDBS footprint. In this sense, BDBS is unique because the project's core goal is understanding > 200 contiguous square degrees of the Galactic bulge by utilizing uniform photometry spanning the *ugrizy* filters.

However, before proceeding to analyse the BDBS CMDs, we first seek to verify data quality using the DECaPS and Pan-STARRS catalogues for comparison. Fig. 12 compares i versus $g - i$ CMDs

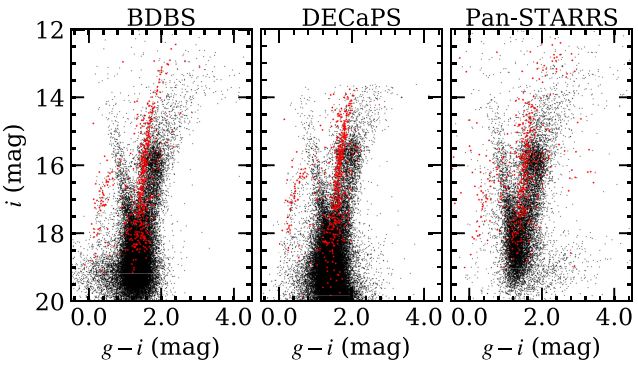

Figure 12. The three panels show i versus $g - i$ CMDs for 5 arcmin regions near the Baade's window globular cluster NGC 6522 using data from BDBS (left), DECaPS (middle), and Pan-STARRS (right). The small black points represent field stars while those shown as filled red points have *Gaia* DR2 proper motions consistent with NGC 6522 membership (Gaia Collaboration 2018b). At least for this field, the DECaPS i-band data are systematically brighter by ∼0.2 mag. than BDBS and Pan-STARRS.

of a region within 5 arcmin of the globular cluster NGC 6522 for the BDBS, DECaPS, and Pan-STARRS catalogues. This particular line-of-sight also resides within the well-studied 'Baade's window' region, which is a low extinction window near $(l, b) \sim (+1, -3.9)$. Although Baade's window is a commonly analysed field for bulge studies, it did not receive any special attention during the calibration procedures for BDBS, Pan-STARRS, or DECaPS. Therefore, the data presented in Fig. 12 should be a fair comparison between the various studies of an effectively random field, which is useful for examining calibration uniformity.

Fig. 12 shows that all three surveys produce morphologically similar CMDs. For example, the blue foreground disc sequences are relatively tight and well separated from the bulge RGB population, but merge with the bulge CMD sequence near $i \sim 18$ mag. Additionally, all three CMDs show a prominent bulge red clump near $i \sim 16$ mag along with a broad RGB that results from a combination of metallicity, distance, and reddening variations. Similarly, the NGC 6522 stars, identified by *Gaia* DR2 proper motions (Gaia Collaboration 2018b), clearly reside on the blue edge of the bulge RGB sequence, which is consistent with the cluster's comparatively low metallicity (Barbuy et al. 2009, 2014; Ness, Asplund & Casey 2014a). The cluster's blue horizontal branch (HB) population is also evident at $g - i < 1$ mag in all three CMDs, and a similar group of field blue HB stars can also be seen.

Despite these similarities, Fig. 12 highlights clear differences between the surveys. The Pan-STARRS data do not reach as deep as BDBS and DECaPS, and the photometric scatter among NGC 6522 stars is noticeably worse. The DECaPS data reach ∼0.5 mag deeper in i compared to BDBS, but since DECaPS did not obtain short exposures the survey has a fainter bright limit compared to BDBS. DECaPS and BDBS exhibit similar photometric precision for the NGC 6522 and field stars that range from $i \sim 14$–20 mag, but the DECaPS red clump appears brighter than those of BDBS and Pan-STARRS. The DECaPS zero-point offset is surprising given that both BDBS and DECaPS are calibrated off of Pan-STARRS. However, Schlafly et al. (2018) note that the DECaPS photometry is systematically brighter relative to Pan-STARRS in more heavily reddened fields.

Fig. 13 shows that for stars with magnitudes ranging from 14 to 18 mag, the median offsets between DECaPS and Pan-STARRS

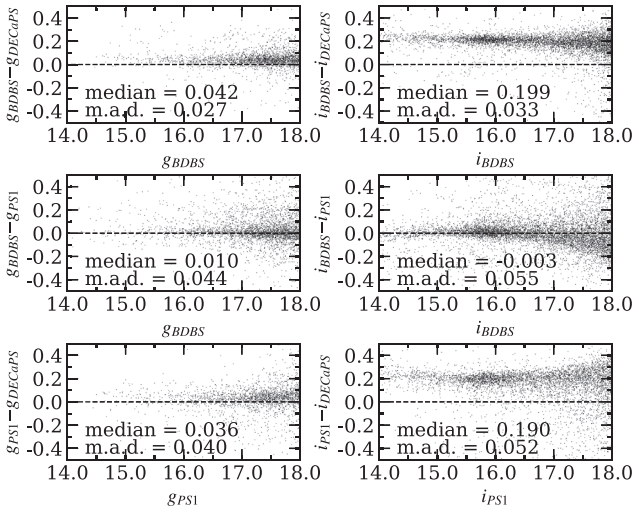

Figure 13. Residual *g*- and *i*-band differences as a function of magnitude are shown for bright stars observed in Fig. 12. For this particular field, the *g*- and *i*-band zero-points are consistent between BDBS and Pan-STARRS (PS1). However, the DECaPS *g* and *i* data appear to be systematically brighter by ∼0.04 and 0.19 mag, respectively. The BDBS and DECaPS data also exhibit some minor structure in the residual plots, which is likely driven by imperfect colour corrections. The median offsets and median absolute deviations are provided for each panel.

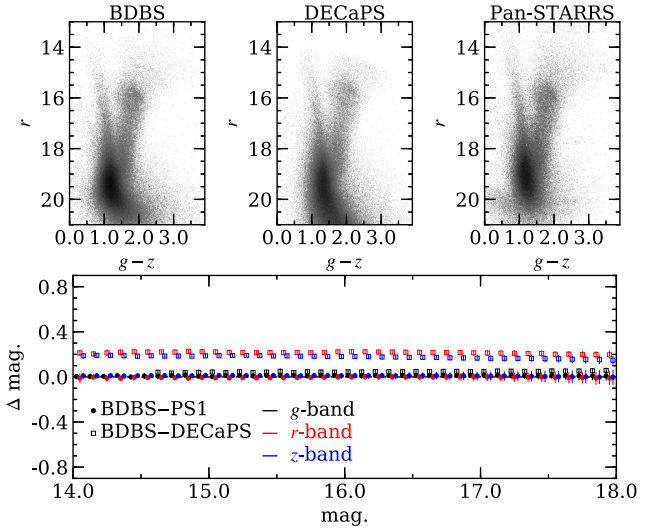

Figure 14. Similar to Fig. 12, *r* versus $g - z$ CMDs are compared between BDBS, DECaPS, and Pan-STARRS for a 20 arcmin field near $(l, b) = (+2, -6)$. Residuals between the three surveys for each filter are shown in the bottom panel with the black symbols illustrating the *g*-band residuals, the red symbols showing the *r*-band residuals, and the blue symbols showing the *z*-band residuals. Since the residuals between BDBS and Pan-STARRS are close to zero, we have omitted the residual points between DECaPS and Pan-STARRS for figure clarity. Note that the symbols represent the median offsets between the surveys in 0.1 mag bins, and that the vertical error bars indicate the median absolute deviations. A comparison between BDBS/Pan-STARRS and DECaPS data shows a systematic offsets of ∼0.05–0.20 mag, depending on the filter.

are 0.036 and 0.190 mag for the *g* and *i* bands, respectively. Similarly, the *g*- and *i*-band offsets between BDBS and DECaPS are 0.042 and 0.199 mag, respectively. By extension the median offsets between BDBS and Pan-STARRS are relatively small at 0.010 and −0.003 mag for *g* and *i*, respectively. Although the median absolute deviations between all three studies do not exceed about 0.05 mag, Fig. 13 shows that both BDBS and DECaPS exhibit a residual systematic offset of $\lesssim 0.1$ mag for stars with $i \gtrsim 17.5$ mag. This residual offset is likely due to higher order terms in the colour corrections, which can also be seen in Fig. 10.

Fig. 14 shows a similar comparison between BDBS, DECaPS, and Pan-STARRS in a less extincted and crowded field near $(l, b) = (+2, -6)$ but for the *grz* filters, and indicates that the BDBS/Pan-STARRS photometry are again in good agreement. The DECaPS data are systematically brighter than BDBS and Pan-STARRS by ∼0.2 mag for the *r* and *z* bands but are within ∼0.05 mag for the *g* band. Although we have only compared two random fields here for data exploration purposes, the evidence suggests that the zero-point correction procedure illustrated in Fig. 8 did an adequate job 'flattening' the data across the BDBS footprint.

4.2 Bulge CMDs and the double red clump

Galactic bulge CMDs can be difficult to interpret due to a variety of effects, including large metallicity spreads, significant differential reddening, and complex line-of-sight geometries related to the inner disc and bar. Increased reddening and crowding also conspire to decrease photometric depth, especially in optical CMDs, for bulge fields close to the plane. These effects are clearly illustrated in the sample BDBS CMDs of Fig. 15 where we note that the Baade's window ($b = -4°$) data reach about 1 mag below the main-sequence turn-off while the minor axis fields at $b \lesssim -6°$ reach another 1–2 mag fainter. Fig. 15 also shows that the apparent magnitude of the red clump is faintest for Baade's window and steadily becomes brighter as the foreground extinction decreases at higher Galactic latitudes.

After applying the reddening corrections illustrated in Fig. 11, as is shown in the bottom panels of Fig. 15, we note that all of the CMDs improve. For example, the red clump apparent magnitude variations disappear, and other important regions, such as the main-sequence turn-off and blue edge of the RGB, now reside at consistent $(g - i)_o$ colours. Additionally, the lower RGBs form tighter sequences and the blue HB populations exhibit reduced photometric scatter. The $b = -4°$ panel of Fig. 15 also shows the 'blue loop' population noted by Saha et al. (2019) at $(g - i)_o \sim 0.75$ and $i_o \sim 12.5$ mag. However, we show in Rich et al. (2020, submitted) that these stars have distances of ∼3 kpc or less, and are therefore likely foreground red clump stars.

Reddening-corrected CMDs, such as those shown in Fig. 15, also permit more detailed morphological examinations. As a verification case, we can explore the red clump regions of the three minor axis fields. Previous studies such as McWilliam & Zoccali (2010) and Nataf et al. (2010) showed that several bulge sightlines with $|b| > 5°$ exhibit two red clumps separated by ∼0.5 mag in the *I* and K_S bands. As mentioned in Introduction, these and other authors contend that the double red clumps trace out an 'X'-shaped structure, and that the two clumps reside at the near (∼6.5 kpc) and far (∼8.8 kpc) ends of the bar. However, other explanations relating to chemical composition variations, particularly involving He enhancements, have also been suggested (e.g. Lee, Joo & Chung 2015; Joo, Lee & Chung 2017; Lee et al. 2018, 2019; López-Corredoira et al. 2019).

Fig. 16 highlights the red clump regions in dereddened CMDs for the same minor axis fields shown in Fig. 15. As expected, the minor axis field near $b = -4°$ exhibits a strong but unimodal red clump at $i_o \sim 15.0$ mag. However, the outer bulge fields at $b = -6°$ and $-8°$ exhibit clear double red clumps separated by ∼0.4–0.5 mag. in the *i* band. This separation is similar to that observed by Nataf et al.

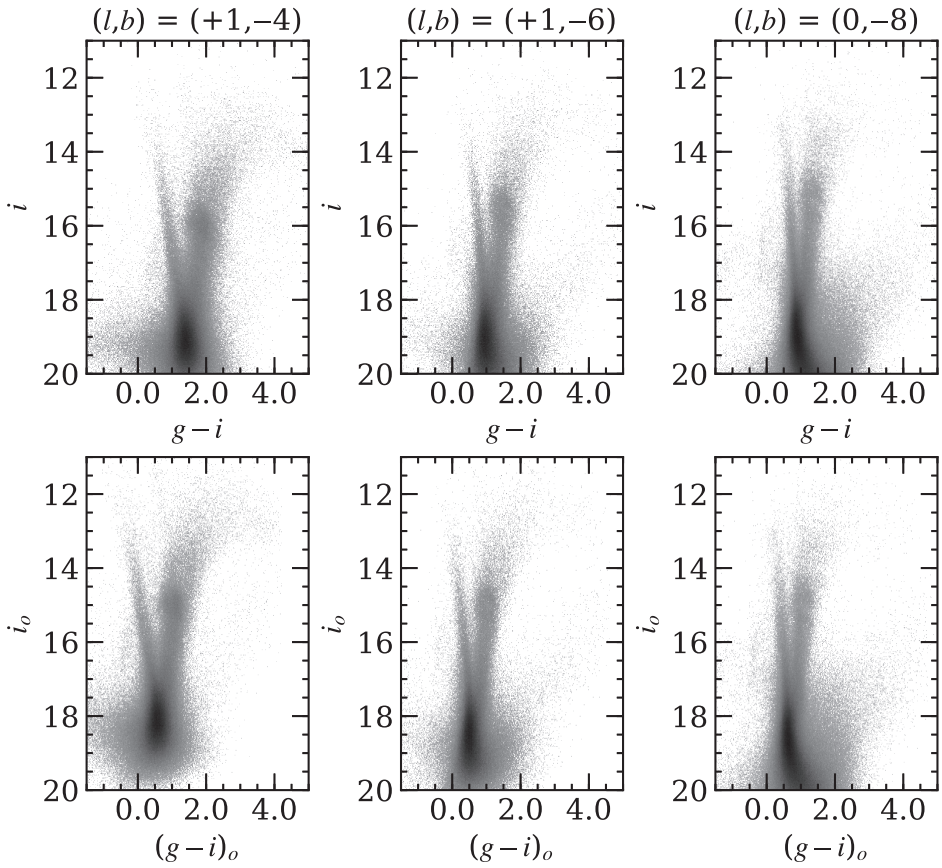

Figure 15. The top panels show binned i versus $g - i$ CMDs for three minor axis fields at varying Galactic latitudes. The bottom panels illustrate the same fields but with reddening corrections from Simion et al. (2017) applied (see the text for details). Note that the $b = -4^\circ$ and -6° fields span a radial distance of 20 arcmin from the noted field centres, while the $b = -8^\circ$ field spans a 40 arcmin radius. All three fields show evidence of blue HB populations, and double red clumps are visible in the $b = -6^\circ$ and -8° fields. The two left-hand panels are comparable to fig. 10 in Saha et al. (2019).

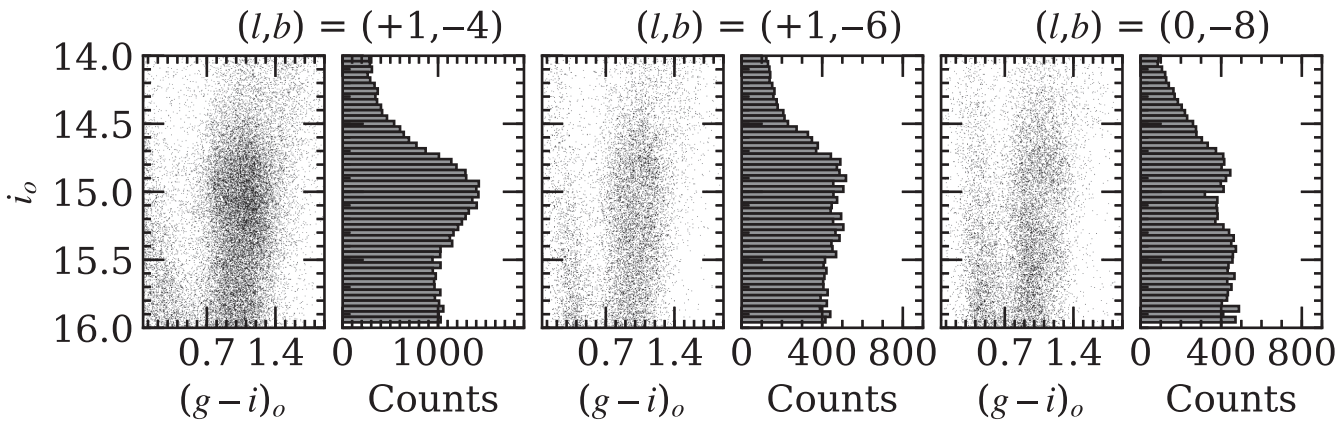

Figure 16. Dereddened i versus $g - i$ CMDs are shown for the same fields as in Fig. 15 with an emphasis on the red clump region. Histograms for each field illustrate the monolithic red clump population in Baade's window that contrasts with the double red clumps, located at $i_o \sim 14.9$ and 15.35 mag, found in higher Galactic latitude fields.

(2010) using OGLE observations. For the $b = -6^\circ$ field, the bright and faint red clumps peak near $i_o = 14.9$ and 15.3 mag, respectively, but the two clumps are found near $i_o = 14.9$ and 15.4 mag in the $b = -8^\circ$ field. The increased brightness separation for higher latitude bulge fields is consistent with the 2MASS K_S-band measurements from McWilliam & Zoccali (2010).

A more detailed examination of the $b = -8^\circ$ field is shown in Fig. 17. The foreground disc, blue HB, double red clumps, and bulge RGB sequences are all well populated. The blue HB is particularly extended and ranges from at least $i_o = 15$–18 mag. Similar features are also present in DECam CMDs involving the *rzy* filters, as is evident in figs 9 and 11 from Saha et al. (2019) and those shown in

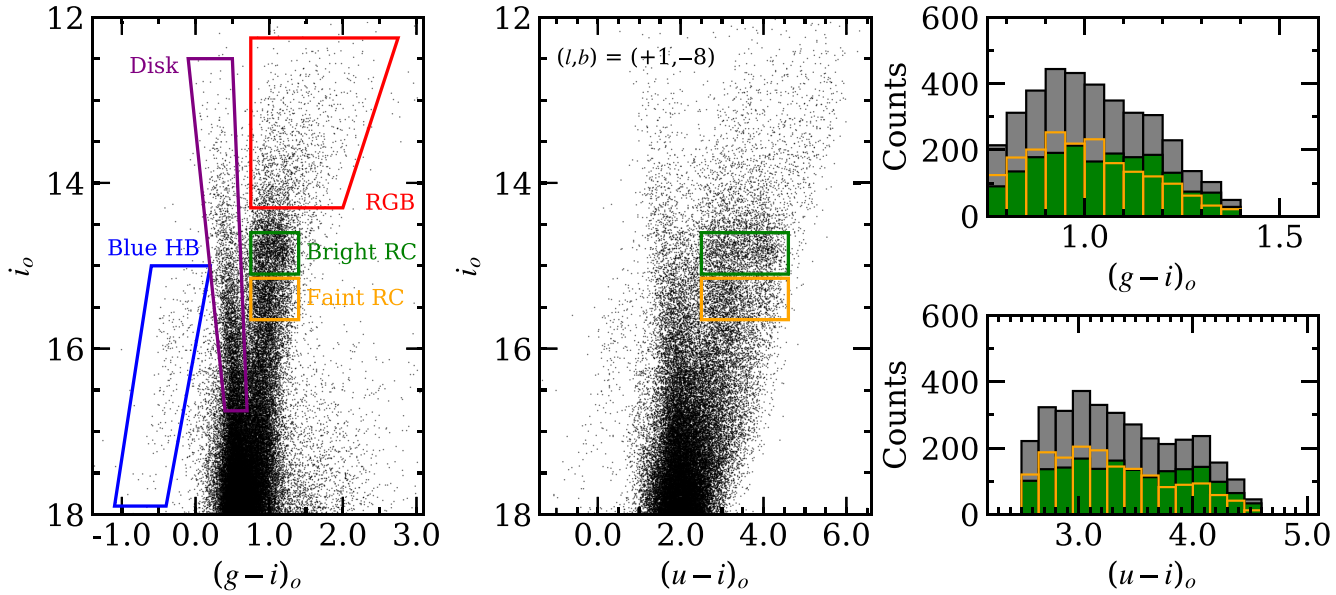

Figure 17. Left: a dereddened i versus $g - i$ CMD for a minor axis field at $(l, b) = (+1, -8)$ with a radius of 20 arcmin. Several CMD features are highlighted, including the RGB, extended blue HB, foreground disc, and bright/faint red clump populations. Middle: a similar CMD using $(u - i)_o$ as the colour base line. The green and orange boxes indicate the locations of the bright and faint red clumps, respectively. Note that the bright and faint red clumps each contain separate populations of 'blue' and 'red' populations. Right: the top and bottom panels show histograms of the red clump populations as functions of $(g - i)_o$ and $(u - i)_o$, respectively. The grey histograms include all red clump stars while those shown in green and orange represent the bright and faint red clumps, respectively. Note the clear bimodal distribution present when using $(u - i)_o$.

Section 4.4 of this work. Fig. 17 also shows that the red clump $(g - i)_o$ dispersion is relatively small, and that the bright and faint red clumps effectively span the same colour range. Interestingly, we find some weak evidence of bimodality in the $(g - i)_o$ red clump histogram, particularly for the bright red clump, which could be indicative of a bimodal metallicity distribution. However, Fig. 17 shows that the u band is a much stronger filter for separating stars by chemical composition.

4.3 The *u*-band and metallicity distribution functions

4.3.1 Red clump colour split

The most striking feature of Fig. 17 is that adding the u-band dramatically increases the colour dispersion of bulge stars on the RGB, which is particularly evident in the red clump region. When plotted using a $g - i$ baseline, the double red clump spans ∼0.6 mag in colour. However, with $u - i$, the two red clumps span >2 mag in colour. Furthermore, the addition of the u band splits each component of the double red clump into two populations that are separated by about 1 mag in $u - i$ (making four in total). The separate blue and red populations are clearly seen as distinct clumps in the i_o versus $(u - i)_o$ panel of Fig. 17, but the ratios of the blue/red populations vary between the bright and faint red clumps.

At least for the $(l, b) = (+1, -8)$ sightline shown in Fig. 17, the bright red clump has a blue fraction of 0.622 ± 0.039 and a red fraction of 0.378 ± 0.046, when separated at $(u - i)_o = 3.65$ mag. Similarly, the faint red clump has blue and red fractions of 0.747 ± 0.038 and 0.253 ± 0.055, respectively. A similar discrepancy between the bright and faint red clumps has been noted by previous authors as well (Ness et al. 2012; Uttenthaler et al. 2012; Rojas-Arriagada et al. 2017), which found the bright red clump to contain a larger fraction of metal-rich stars compared to the faint red clump distributions.

4.3.2 Linking the u *band with metallicity*

The colour split on the RGB, and particularly in the red clump region, is a common feature seen in the BDBS i_o versus $(u - i)_o$ CMDs. Furthermore, the observed CMDs (i.e. not corrected for reddening) in outer bulge fields where the extinction is much lower (e.g. see Fig. 11) are morphologically similar to the dereddened versions, and suggest that the $u - i$ red clump colour dispersions and discrete populations, such as those seen in Fig. 17, result from physical differences between stars rather than poor reddening corrections. The DECam u band spans approximately 3500–4000 Å in wavelength, which is a region that includes numerous strong metal lines in red clump stars. As a result, more metal-rich stars will have increased line blanketing and appear significantly redder in $u - i$ than their more metal-poor counterparts.

We can verify that the $u - i$ colour dispersion is driven by metallicity via direct comparison with the GIRAFFE Inner Bulge Survey (GIBS) data base, which reported [Fe/H] values for several thousand red clump stars in sightlines that largely overlap with BDBS. Metallicity variations as a function of CMD location for three BDBS fields are shown in Fig. 18 and indicate that $(u - i)_o$ is strongly correlated with [Fe/H]. Additionally, Fig. 18 shows that the colour–metallicity relations are nearly identical across the 15 calibration sightlines, and are also independent of whether stars are in the bright or faint red clumps. Therefore, we determined a global red clump colour–metallicity relation for BDBS as:

$$[\mathrm{Fe/H}] = 0.563(u - i)_o - 2.074, \quad (22)$$

where [Fe/H] is the calibrated iron abundance for a star and $(u - i)_o$ is the dereddened BDBS colour. The typical scatter in [Fe/H] when using the derived colour–metallicity relation is ∼0.2 dex or better, and is probably limited by the accuracy of the GIBS metallicities, along with the resolution and accuracy of the reddening map.

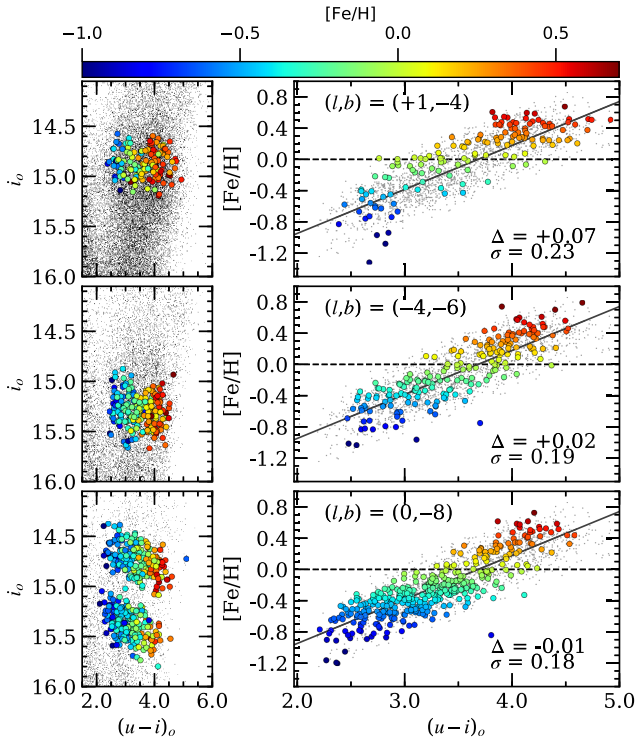

Figure 18. Left: dereddened i versus $u - i$ CMDs centred in the red clump region are shown for three bulge fields. The large filled circles are red clump stars from GIBS (Zoccali et al. 2017) that have spectroscopic [Fe/H] determinations. The colours indicate each star's [Fe/H] value and are saturated at [Fe/H] = −1.0 (blue) and +0.7 (red). Note the strong dependence of $(u - i)_o$ on stellar metallicity. Right: plots of [Fe/H] versus $(u - i)_o$ are shown for the three fields. The small grey circles illustrate the trend of all 14 GIBS fields used here, and the best-fitting linear relation is shown with the solid dark grey line. The mean offsets (Δ) between the observed and predicted [Fe/H] values, along with the standard deviations (σ), are provided for each field.

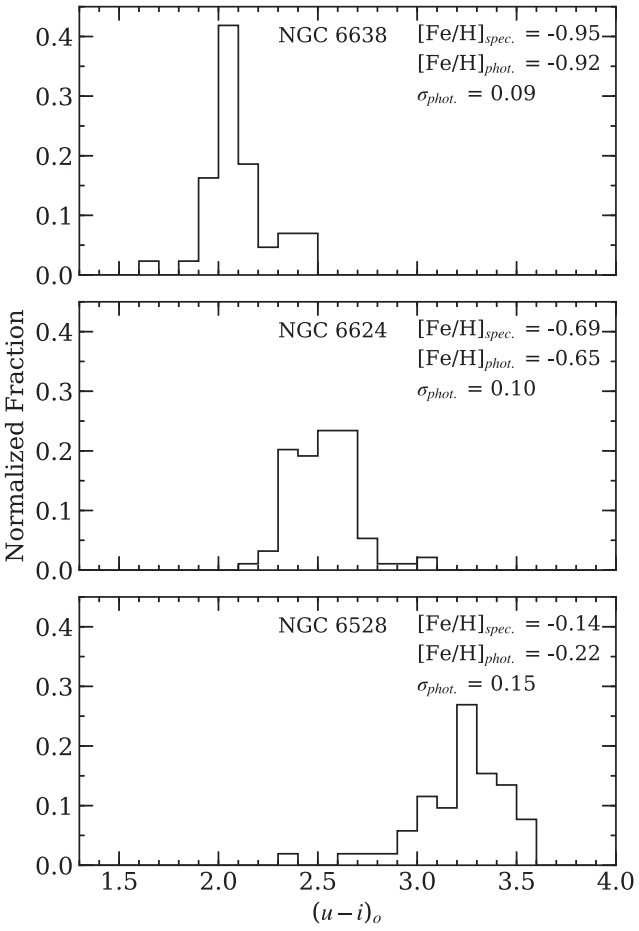

Figure 19. Binned histograms illustrating the red clump $(u - i)_o$ distributions are shown for three well-sampled BDBS globular clusters that span [Fe/H] ∼ −1 to −0.1. Each histogram includes only stars that could be clearly separated from the cluster RGB, had *Gaia* DR2 proper motions consistent with cluster membership, and were bluer than the RR Lyrae region. The spectroscopic [Fe/H], photometric [Fe/H], and photometric [Fe/H] dispersion are provided for each cluster. Despite some increased colour dispersion due to factors such as mass loss, rotation rate, and light element abundance variations, the $(u - i)_o$ distribution is strongly peaked for each cluster and becomes redder at higher [Fe/H]. Spectroscopic metallicities for NGC 6638, NGC 6624, and NGC 6528 are from Mauro et al. (2014), Valenti, Origlia & Rich (2011), and Muñoz et al. (2018), respectively.

As an independent verification that $(u - i)_o$ is correlated with [Fe/H], Fig. 19 shows histograms of the $(u - i)_o$ distributions for red clump stars in three bulge globular clusters. The clusters NGC 6638, NGC 6624, and NGC 6528 were chosen because they span about a factor of 10 in [Fe/H], have well-sampled red HB populations, reside within the BDBS reddening map region, and have literature spectroscopic [Fe/H] measurements. Using the colour–metallicity relation provided in equation (22), Fig. 19 indicates that: the mean red clump colour becomes redder at higher metallicity, the mean photometric [Fe/H] estimate is within 1σ of the spectroscopic value, and the dispersion around the mean is approximately 0.1–0.15 dex. Therefore, we conclude that $(u - i)_o$ is an accurate tracer of metallicity in old red clump stellar populations.

Although similar colour–metallicity relations could be derived for brighter RGB stars, red clump stars are generally more useful because their absolute magnitudes are relatively well constrained. RGB-tip stars have been used in the past to calculate metallicity distribution functions with both optical (e.g. Zoccali et al. 2003; Johnson et al. 2011) and near-IR (e.g. Gonzalez et al. 2013) data. However, since the [Fe/H] estimates using this isochrone method are functions of colour *and* magnitude, distance uncertainties can significantly affect a star's assumed metallicity. Additionally, degeneracy in the colour–metallicity relation can be large because the optical/near-IR colour dispersion is relatively small until the last few tenths of a magnitude near the RGB-tip.

Recently, Mohammed et al. (2019) combined *GALEX NUV* photometry with *Gaia G*-band magnitudes and performed a similar colour–metallicity calibration for nearby red clump stars based on APOGEE abundances; however, despite the $NUV - G$ colour having a larger dispersion for red clump stars than $u - i$, this method likely has limited utility in bulge fields. For example, *GALEX NUV* magnitudes have a much stronger dependence on extinction than the u band, and such observations would have to reach at least $NUV \sim$ 24–25 mag with reasonable S/N to be useful in the bulge. The limit would be fainter in even moderately extincted fields. *GALEX* pixels are also several times larger than those of DECam, which strongly affects photometry in crowded fields. We conclude that $u - i$ is a superior colour for photometrically measuring the metallicities of red clump stars in crowded bulge fields, and with a typical uncertainty of ∼0.2 dex our calibration is comparable in precision to spectroscopic methods such as the Calcium Triplet.

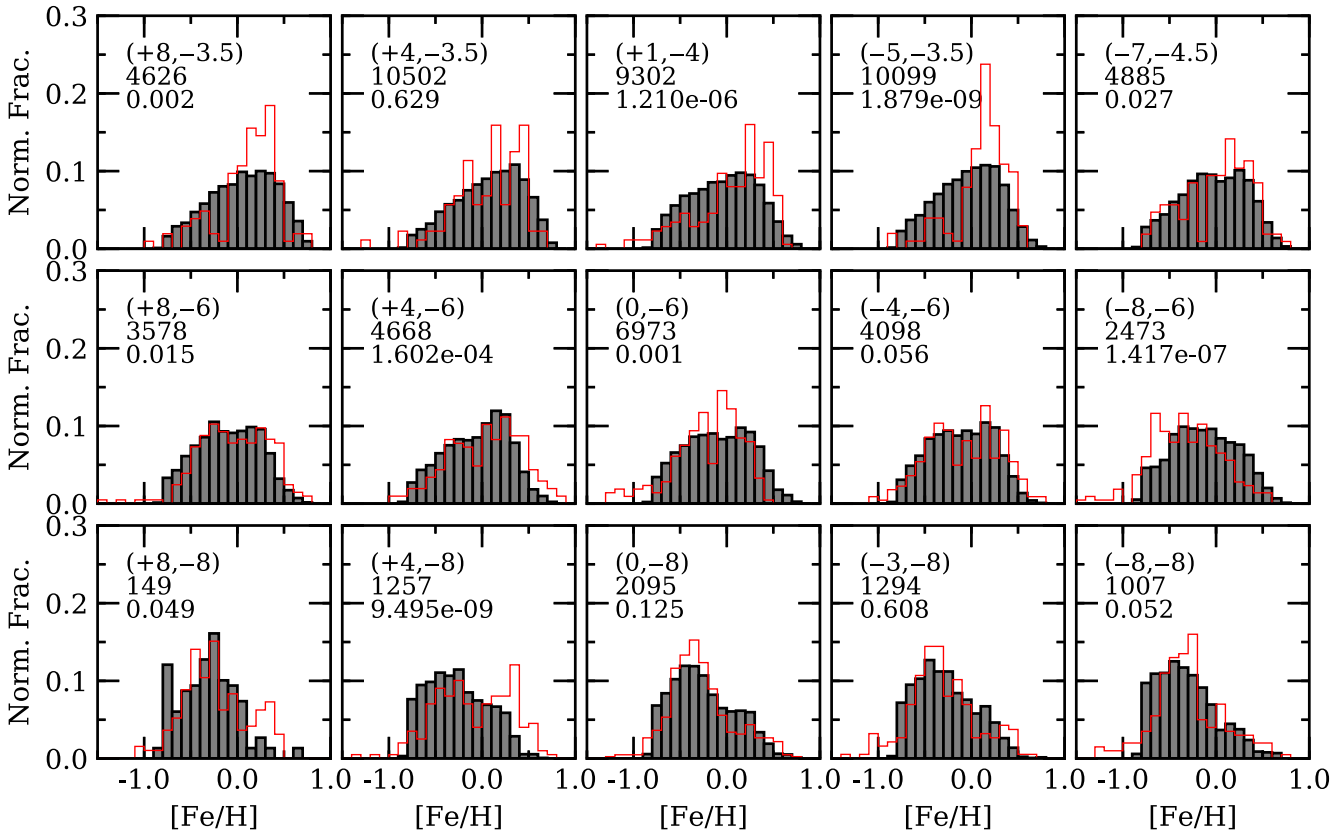

Figure 20. Similar to fig. 4 in Zoccali et al. (2017), we compare the metallicity distribution functions of red clump stars in BDBS (filled grey histograms), derived using the colour–[Fe/H] relation shown in Fig. 18, with those of GIBS (red histograms). The Galactic coordinates, number of BDBS red clump stars, and p-value of two-sided KS tests are provided in each panel. Each BDBS field spans approximately 15 arcmin in radius.

Although we have shown that $(u - i)_o$ correlates with stellar metallicity, we stress several important caveats related to photometric [Fe/H] measurements and interpretations of the bulge's physical structure. First, core He-burning stars with [Fe/H] $\lesssim -1$ tend to reside on the blue HB rather than the red clump, which means our analysis is biased against the most metal-poor stars. Fortunately, an overwhelming majority of stars in the bulge have $-0.8 \lesssim$ [Fe/H] $\lesssim +0.5$. Additionally, many stars with [Fe/H] < -1 that are projected on to the bulge are likely to be halo interlopers.

A second and more significant problem relates to the contamination rate and evolutionary state uncertainty of stars residing in the red clump region of bulge CMDs. The most obvious contaminant is the exponential background of first ascent RGB, plus some AGB (asymptotic giant branch), stars that can overlap in colour and magnitude with the red clump. This simple background can account for as many as 20–30 percent of stars in the red clump region (e.g. Nataf et al. 2011; Clarke et al. 2019). Since red clump stars are bluer than RGB stars of the same metallicity, the RGB stars will follow a different colour–metallicity relation. However, as extensively described by Nataf, Cassisi & Athanassoula (2014), quantifying the contaminating RGB population is difficult because metallicity, He abundance, and distance variations modify the colours, magnitudes, and evolutionary lifetimes of RGB, red clump, and AGB stars. In the future, the red clump colour–metallicity relation may be improved using a combination of asteroseismology, parallax distances, and proper motions to isolate samples of pure red clump stars residing at bulge distances.

4.3.3 Metallicity distribution functions

As mentioned in Introduction, the metallicity distribution function is an important tool for understanding the formation history of stellar populations. However, little agreement exists regarding the true nature of the bulge's metallicity distribution (e.g. see review by Barbuy et al. 2018). For example, early work by Rich (1990) showed that the inner bulge was well described as a unimodal population that largely followed the expected distribution from a one-zone closed box enrichment model. In contrast, more recent measurements claim that the bulge is a multi component system hosting anywhere from 2 to 5 distinct populations (e.g. Hill et al. 2011; Ness et al. 2013a; Bensby et al. 2017; Rojas-Arriagada et al. 2017; Zoccali et al. 2017; García Pérez et al. 2018; Duong et al. 2019). Most authors also find that fields closer to the plane are dominated by metal-rich stars while those farther from the plane host more metal-poor stars. Additional metal-poor populations with [Fe/H] < -1 have also been detected (e.g. García Pérez et al. 2013; Ness et al. 2013a; Koch et al. 2016), but many of these stars are likely halo interlopers.

Fig. 20 summarizes the derived metallicity distribution functions for the 15 calibration fields that total $> 67\,000$ red clump stars. The distributions are largely compatible with previous analyses that found a vertical metallicity gradient, driven by the changing ratios of metal-poor and metal-rich stars, along with at least two 'peaks' in several, especially outer, bulge fields (e.g. Zoccali et al. 2008; Babusiaux et al. 2010; Ness et al. 2013a; Gonzalez et al. 2015; Rojas-Arriagada et al. 2017; Zoccali et al. 2017). However, Fig. 20 indicates that fields interior to $b \sim -6°$, and reaching at least the $b \sim -3.5°$ limit shown

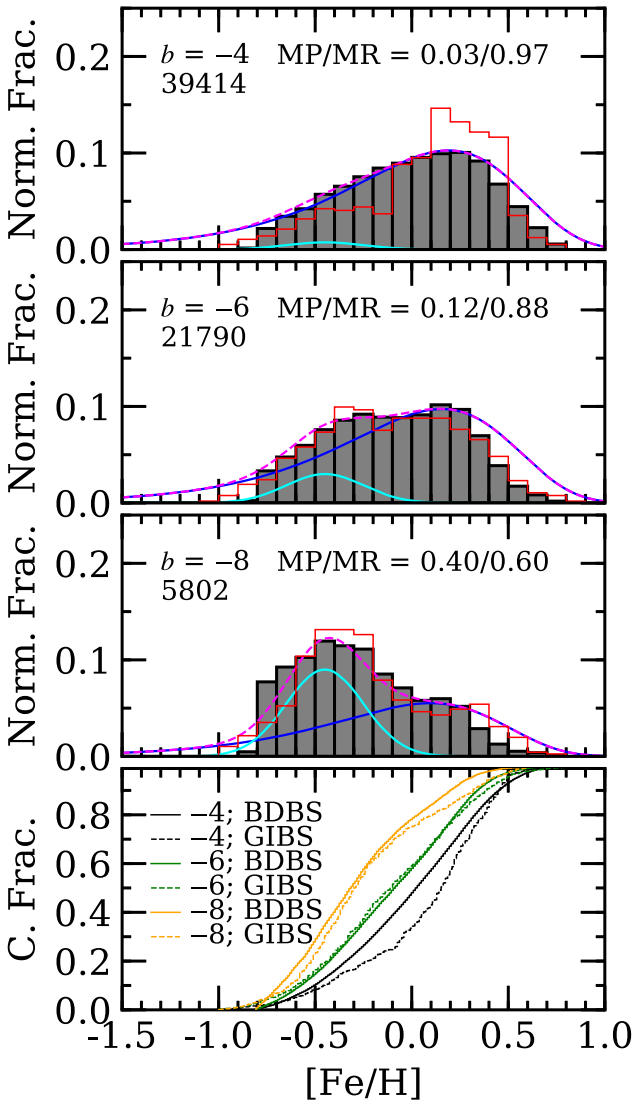

Figure 21. Similar to fig. 7 in Zoccali et al. (2017), the [Fe/H] distributions from Fig. 20 for BDBS (grey bars) and GIBS (red lines) have been summed across each Galactic latitude segment and are presented as histograms in each panel. The Galactic latitude and number of BDBS red clump stars are provided in each panel. The solid blue lines show the expected distributions for a one-zone closed box gas exhaustion model with a mean effective yield of [Fe/H] $\sim +0.15$. The solid cyan lines illustrate the addition of a metal-poor, normally distributed component with $\langle$[Fe/H]$\rangle = -0.45$ and $\sigma = 0.25$, and the dashed magenta lines show the combined closed box and normal components. The area ratios of metal-poor (cyan) and metal-rich (blue) are provided in each panel. The bottom panel compares the same data but as a cumulative distribution functions for the $b = -4^\circ$ (black), $b = -6^\circ$ (green), and $b = -8^\circ$ (orange) BDBS (solid lines) and GIBS (dashed lines) fields.

here, do not necessarily possess a significant additional metal-poor component.

Fig. 21 sums across the fields at fixed Galactic latitudes and shows that the $b = -4^\circ$ sightlines are morphologically similar to the expected distribution from a simple closed box gas exhaustion model of the form:

$$\frac{dN}{d[Fe/H]} \propto 10^{[Fe/H]} e^{-\frac{10^{[Fe/H]}}{y}}, \quad (23)$$

where y is the mean effective yield (e.g. Searle & Zinn 1978; Rich 1990). Distributions described by equation (23) are unimodal but strongly asymmetric with long metal-poor tails. Similarities between closed box models and bulge metallicity distributions have been noted before (e.g. Rich 1990; Zoccali et al. 2003, 2008), but more recent investigations have dropped this model in favour of fitting multiple Gaussian functions. Although such an approach is convenient for population studies and fitting, little physical motivation exists regarding why the bulge should be a composite of two or more populations that each have a relatively narrow, normally distributed metallicity distribution function. Systems composed of two or more populations with narrow, normally distributed metallicity distributions do exist in nature, but such objects often show extreme heavy element abundance variations that are indicative of a prolonged period of 'bursty' star formation and self-enrichment, particularly from low- and intermediate-mass AGB stars (e.g. ω Cen; Johnson & Pilachowski 2010; Marino et al. 2011b). The Galactic bulge shows no evidence supporting this type of enrichment pattern (e.g. Johnson et al. 2012; Van der Swaelmen et al. 2016; Bensby et al. 2017; Duong et al. 2019), although its physical parameters also differ substantially from those of 'iron-complex' globular clusters.

At least for $b = -4^\circ$, fitting equation (23) to the BDBS data only leaves room for an additional metal-poor component at the few per cent level. Although the simple closed box model follows the general shape of the observed $b = -4^\circ$ distribution, we note some differences in the metal-poor and metal-rich tails. For the metal-poor tail, BDBS does not find as many stars as the model predicts. However, the paucity of BDBS stars with [Fe/H] < -1 is likely driven by our selection function and the general evolution of metal-poor stars to land on the blue HB. At the metal-rich end, Fig. 21 also shows a steeper drop off than the model, but we suspect that this discrepancy is driven by limitations of the simple model. A truncated metal-rich tail could be accounted for by an improved model, such as one that includes gas outflow. Nevertheless, the cumulative distribution functions at $b = -4^\circ$ in Fig. 21 for BDBS and GIBS do not exhibit well-defined inflection points that would be indicative of strongly bimodal distributions.

For the fields at $b = -6^\circ$ and -8°, Fig. 21 does confirm previous claims that a secondary metal-poor population is found near [Fe/H] ~ -0.4. However, following the assumption that the metal-rich peak is a tracer of the same underlying population that dominates at $b = -4^\circ$, we find the secondary metal-poor component to be much weaker than previous estimates. For example, Zoccali et al. (2017) found that the metal-poor populations constitute 51 and 73 per cent of the stars at $b = -6^\circ$ and -8°, respectively. In contrast, we find in those same fields that the secondary metal-poor component only contributes about 10 and 40 per cent of the total star counts, respectively.[14] We urge caution when force fitting multiple Gaussian functions to bulge metallicity distributions, since Fig. 21 highlights that a significant fraction of bulge stars could follow an inherently skewed and non-normal distribution.

Sampling issues also remain an important consideration, and in this sense further insight may be gained from the $(l, b) = (+4, -3.5)$ panel in Fig. 20. For this field, Zoccali et al. (2017) fit two Gaussian distributions with mean [Fe/H] values of ~ -0.2 and $+0.3$. However,

[14]Since the red clump does not strongly sample stars with [Fe/H] < -1, we do not have enough information to estimate the underlying shape of the separate metal-poor component. Lacking compulsory evidence, we assume a Gaussian distribution. However, depending on the origin of the metal-poor component, it could have a different functional form.

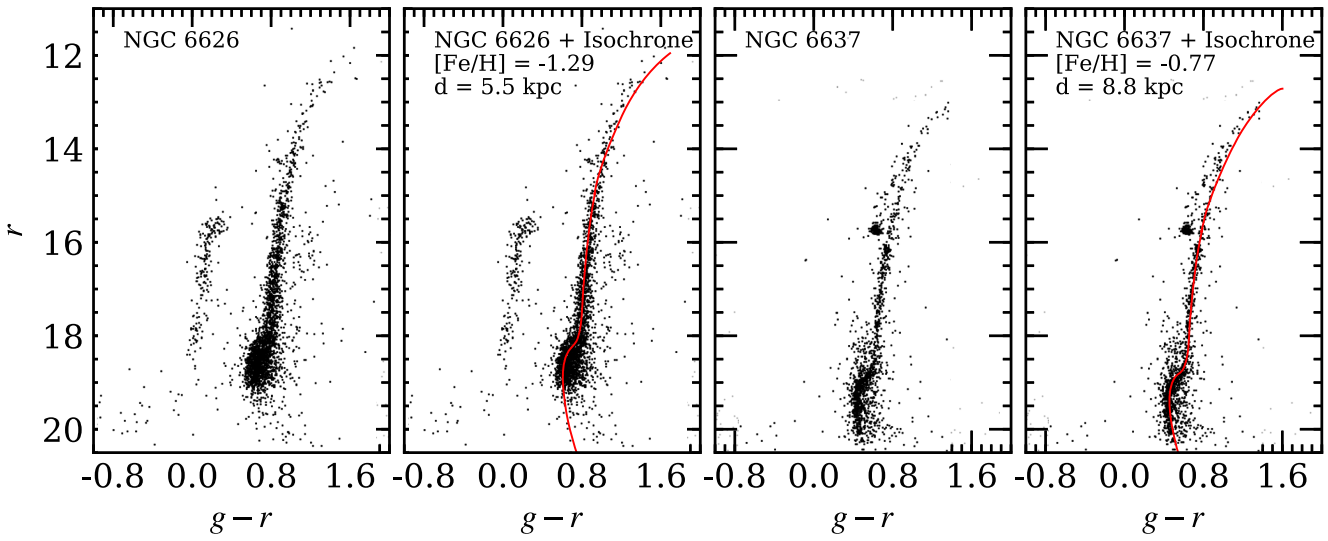

Figure 22. Sample r versus $g - r$ CMDs are shown for the bulge globular clusters NGC 6626 (left two panels) and NGC 6637 (right two panels), which have completely blue and red HBs, respectively. The light grey symbols include all stars within 5 arcmin of the cluster centres and the black symbols indicate stars that also have proper motions consistent with cluster membership. Isochrones (Girardi et al. 2000) are overplotted (solid red lines) for both clusters assuming ages of 12.5 Gyr and $[\alpha/\mathrm{Fe}] = +0.3$, along with the listed [Fe/H] and distance values from Villanova et al. (2017) and Lee & López-Morales (2007). $E(B-V)$ values of 0.40 and 0.18 mag (Harris 1996) were applied to the NGC 6626 and NGC 6637 isochrones, respectively.

the BDBS data show a clear peak near [Fe/H] $\sim +0.25$ but do not show evidence of a local maximum at lower metallicity. A two-sided Kolmogorov–Smirnov (KS) test returns a p-value[15] of 0.629 when comparing the BDBS and GIBS [Fe/H] distributions, but the 120× larger sample in BDBS appears to smooth out other potential modes. Similarly, we note that the BDBS and GIBS distributions, as traced by the KS-test p-values in Fig. 20, may become more similar in the lower density outer bulge regions. Since the GIBS project observed ∼200 stars per field, regardless of the local stellar density, the metallicity histograms presented in Zoccali et al. (2017) sample progressively smaller fractions of the underlying distributions at lower latitudes. Nevertheless, the BDBS fields also suffer from a variety of contamination issues (see Section 4.3.2) that will require further detailed analyses to fully disentangle.

4.4 Globular cluster CMDs

An additional area of inquiry for data validation and exploration with BDBS is globular cluster CMDs. As shown in Fig. 1, BDBS includes at least 25 Galactic globular clusters that span a variety of masses, metallicities, and HB morphologies. For example, Fig. 22 shows r versus $g - r$ CMDs for the globular clusters NGC 6626 ([Fe/H] ~ -1.3) and NGC 6637 ([Fe/H] ~ -0.77), which have almost completely blue and red HB morphologies, respectively. For both clusters, BDBS easily reaches below the main-sequence turn-off and also samples the RGB-tip. Additional key evolutionary indicators, such as the RGB-bump and AGB, are also readily visible in Fig. 22.

A comparison with isochrones from Girardi et al. (2000) indicates that the BDBS globular cluster CMDs are well calibrated on to the Pan-STARRS system, and that the evolutionary sequences follow the expected distributions. The small star-to-star scatter along the RGB sequences also indicate that the photometric precision is stable over a wide magnitude range. Furthermore, we do not detect any systematic variations in colour or magnitude between 'bright' and 'faint' stars that would have been preferentially measured in the long, short, or ultrashort exposures.

Fig. 22 also shows the crowding and magnitude limitations of *Gaia* DR2 (Gaia Collaboration 2018a) in the bulge region. For NGC 6626, which has a Galactic latitude of $-6°$, Gaia DR2 proper motions are only useful for finding cluster members down to $r \sim 19$ mag. However, in the less crowded NGC 6637 field at $b \sim -10.3°$ *Gaia* DR2 proper motions can distinguish cluster members down to $r \sim 20$ mag. In both cases BDBS reaches at least 1–2 mag deeper than *Gaia*. Future *Gaia* data releases will likely permit BDBS globular cluster investigations reaching down to the lower main sequence in most clusters. We now use BDBS data to briefly investigate three additional globular clusters that have disputed properties.

4.4.1 NGC 6656 (M 22)

NGC 6656 is one of the most massive globular clusters in the Milky Way and is thought to be the remnant core of a former dwarf spheroidal galaxy. A key indicator of the cluster's peculiarity is its metallicity distribution function, which shows a significant spread or bimodality that also coincides with variations in elements produced by the slow neutron-capture process (Da Costa et al. 2009; Marino et al. 2009; Lee 2016). Combined near-UV and optical CMDs show that NGC 6656 has a double subgiant branch (SGB), and that stars on the two branches have different heavy element abundances (Piotto 2009; Marino et al. 2012). However, Mucciarelli et al. (2015) claim that only elements produced by the slow neutron-capture process show variations in the cluster and that NGC 6656 has a negligible [Fe/H] spread.

In Fig. 23, we utilize our DECam *ugri* photometry to investigate whether the split SGB is recovered in BDBS CMDs. First considering i versus $g - i$, Fig. 23 shows that a SGB colour/luminosity spread is not easily detected using these filter combinations, despite both BDBS and *Gaia* data providing a clean separation between the cluster and field stars well below the main-sequence turn-off. Comparing

[15]We adopt the common convention that a p-value < 0.05 is sufficient to reject the null hypothesis.

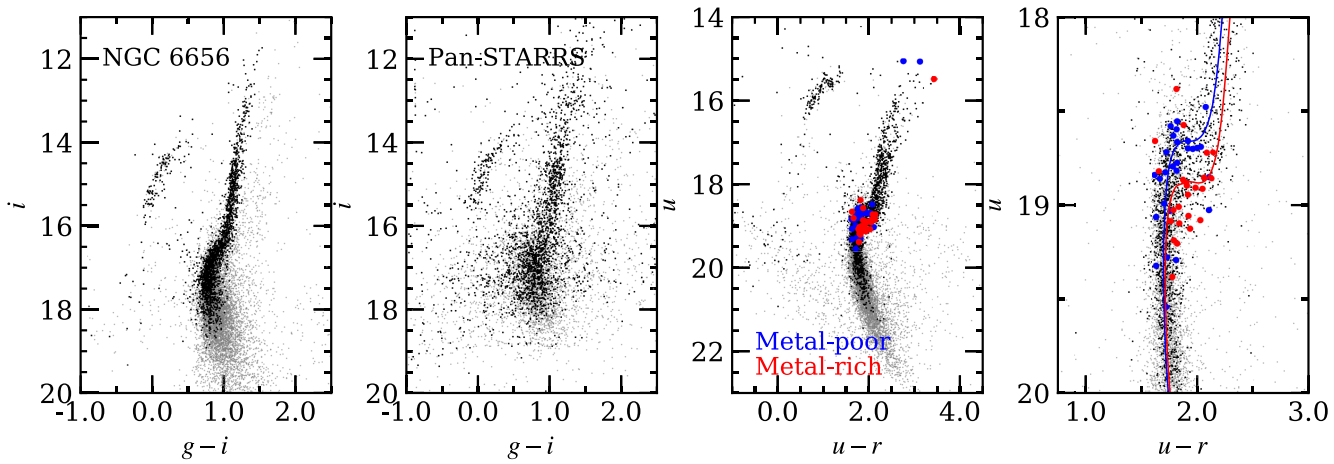

Figure 23. Several BDBS CMDs are shown for stars within one half-light radius (3.36 arcmin) of the globular cluster NGC 6656 (M 22). The light grey circles indicate all stars within a half-light radius, while the black circles show objects that also exhibit *Gaia* DR2 proper motions consistent with cluster membership. For comparison, the middle left CMD includes stars with the same spatial and proper motion selection criteria as the left-hand panel, but only uses data from Pan-STARRS. The two right-hand panels include metal-poor (s-poor) and metal-rich (s-rich) stars from Marino et al. (2009, 2011a, 2012) as blue and red circles, respectively. The blue and red solid lines illustrate 12 Gyr, α-enhanced isochrones with [Fe/H] $= -1.85$ (blue) and -1.65 (red) from Dotter et al. (2008). Note that the isochrones and split SGB are consistent with a bimodal metallicity distribution for the cluster.

with an equivalent Pan-STARRS i versus $g - i$ CMD for NGC 6656 reinforces that optical and near-IR colours are not optimal for detecting small metallicity variations in the SGB region of old, metal-poor globular cluster populations. However, the comparison does highlight the superior performance of BDBS compared to Pan-STARRS for bulge globular cluster CMD analyses as BDBS reaches at least 1–2 mag deeper and has smaller photometric scatter.

When the u and r bands are combined, Fig. 23 illustrates that both the SGB and RGB split into two broadened sequences. To verify that the split SGB/RGB sequences are tracers of metallicity variations, we matched BDBS to the spectroscopic results of Marino et al. (2009, 2011a, 2012). The result shown in Fig. 23 indicates that the split SGB/RGB using u versus $u - r$ CMDs does follow the metallicity variations determined via spectroscopy. The effect is particularly clear on the SGB where we find that stars in the 'metal-poor' NGC 6656 group overwhelmingly reside on the brighter SGB while those in the 'metal-rich' group trace the faint SGB. A comparison with isochrones from Dotter et al. (2008) further reveals that the magnitude of the SGB split aligns with those predicted from stellar evolution theory. These results follow the findings of Marino et al. (2012, see their fig. 11) and confirms that the BDBS u-band data are useful for measuring composition variations in both bulge red clump stars and SGB/RGB stars in globular clusters.

Given the large footprint covered by BDBS, we can also investigate the possible existence of extratidal cluster members. For example, in Fig. 24, we examine a region within 6° of NGC 6656, or at least out to the edges of our survey, to search for stars that have colours, magnitudes, and *Gaia* DR2 proper motions consistent with cluster membership. Since the foreground disc and bulge RGB span a wide range of the CMD, we have restricted the search to only include stars that would be on the upper RGB or blue/extreme HB. We also calculated the orbit of NGC 6656 using the Gala orbit integrator (Price-Whelan 2017) in order to aid the search for any tidal streams.

Kunder et al. (2014) used data from the Radial Velocity Experiment DR4 (Kordopatis et al. 2013) and found only one possible extratidal star that had a colour, magnitude, radial velocity, and chemical composition consistent with cluster membership. Unfortunately, this star resides outside the BDBS footprint and we are unable to verify whether it would have been detected using the methods presented in Fig. 24. However, we do find numerous RGB and HB stars that have CMD locations and proper motions consistent with cluster membership. Fig. 24 does not show any strong evidence of a dense stream associated with NGC 6656, but we do note that many extratidal candidates lie along the projected orbit. A radial velocity and chemical composition analysis of these stars would help confirm their status as former cluster members. Nevertheless, Fig. 24 illustrates the utility of BDBS, especially when combined with *Gaia*, to search for extended stellar structures.

4.4.2 NGC 6569

NGC 6569 is a moderately metal-rich globular cluster ([Fe/H] ~ -0.85) residing $\sim$3 kpc from the Galactic centre, and is particularly interesting because Mauro et al. (2012) found evidence of a double red clump using near-IR VVV data. Such a discovery is important because the bulge cluster Terzan 5, which hosts at least 2–3 populations with different [Fe/H] values, was initially recognized as peculiar due to the detection of a double red clump (Ferraro et al. 2009). However, Mauro et al. (2012) noted that the double red clump feature was only prominent in near-IR CMDs and was not present in optical colours. Johnson et al. (2018) obtained high-resolution spectra for several hundred stars in NGC 6569, including those in both the bright and faint red clumps, but did not find any evidence supporting a metallicity spread nor a light element composition difference between the bright and faint red clump stars. Johnson et al. (2018) concluded that the stars in both clumps were radial velocity members, but was not able to determine whether the near-IR double red clump feature was real.

Therefore, in Fig. 25, we utilize various colour combinations in all six filters to determine if any evidence exists to support the double red clump claim by Mauro et al. (2012). In order to identify stars belonging to the bright ($K_S \sim 14.25$ mag) and faint ($K_S \sim 14.35$ mag) HB populations from Mauro et al. (2012), we first generated a catalogue of BDBS stars within a radius of 5 arcmin of the cluster centre. We then culled the catalogue to retain only stars that had *Gaia* DR2 proper motions that were consistent with cluster membership. Finally, this cleaned list was matched with VVV so that BDBS stars residing within the bright and faint HB selection boxes of Mauro

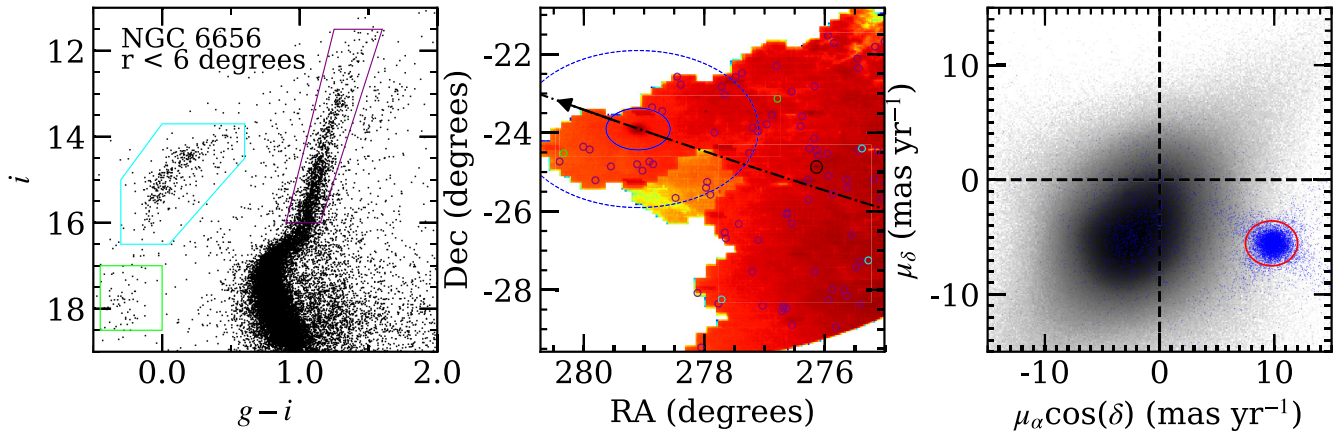

Figure 24. Left: an i versus $g - i$ CMD for BDBS stars within 6° of NGC 6656 that also exhibit proper motions consistent with cluster membership. The purple, cyan, and green regions outline the cluster's RGB, blue HB, and extreme HB populations. Middle: a source density map for the BDBS footprint within 6° of NGC 6656. The solid and dashed blue lines indicate the King (31.9 arcmin) and Wilson (119.9 arcmin) tidal radii from Kunder et al. (2014), respectively. The open purple, cyan, and green circles indicate possible RGB, blue HB, and extreme HB extratidal stars that lie within the selection boxes in the left-hand panel and have proper motions consistent with cluster membership. The large open black circle shows the position of NGC 6626 (M 28). The dotted–dashed black line and arrow indicate the orbital motion of NGC 6656 derived using *Gaia* DR2 proper motions. Note that stars inside the King tidal radius are not plotted. Right: a *Gaia*-based vector point diagram for all BDBS stars within 6° of NGC 6656 (shaded region) along with all stars within one half-light radius (blue circles). The large red circle indicates the proper motion selection region for cluster membership.

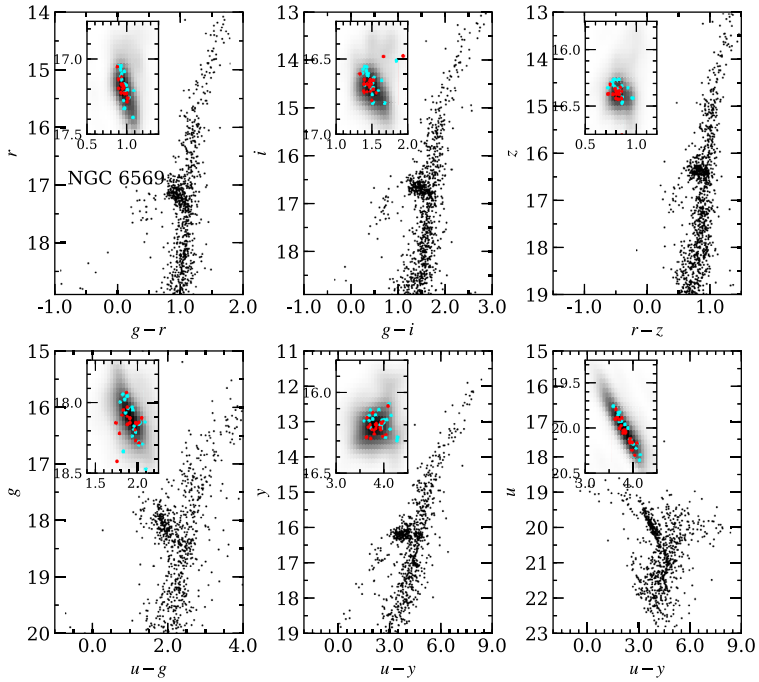

Figure 25. Several BDBS CMDs using multiple filter combinations are shown for the bulge globular cluster NGC 6569. All CMDs include stars within 5 arcmin of the cluster centre that also exhibit *Gaia* DR2 proper motions consistent with cluster membership. The inset figures for each panel are an expansion around the red HB population. The grey scale density map includes all stars within the inset figure boundaries, while the cyan and red open circles indicate individual red HB stars that belong to the 'bright' ($K_S \sim 14.25$) and 'faint' ($K_S \sim 14.35$) HB populations identified by Mauro et al. (2012). The BDBS CMDs do not show any particularly strong evidence supporting a double red HB, with the exception of marginal detections in the z and y bands.

et al. (2012) could be identified. These potential double red clump stars are shown as cyan (bright) and red (faint) circles within the inset CMDs of Fig. 25.

Visual inspection of Fig. 25 suggests that effectively no difference in brightness exists between the bright and faint red HB stars for the *ugri* bands. This assertion is supported by the results of a Welch's t-test comparing the magnitude distributions in each band, which returned p-values of 0.867, 0.658, 0.961, and 0.287 for the *ugri* bands, respectively. However, marginal detections of systematic differences in the mean magnitudes of the z- and y-band distributions were found, and the Welch's t-tests returned p-values of 0.047 and 0.053, respectively.

Fig. 26 illustrates the median magnitude differences between the bright/faint HB populations for each filter, including the VVV K_S band. The data show a small but likely real increase in the magnitude differences between the bright and faint HB populations

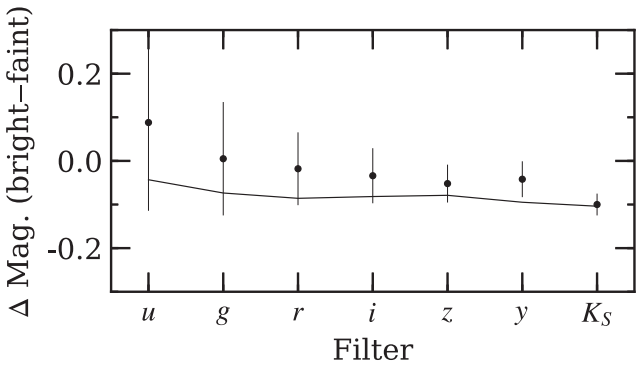

Figure 26. Measured magnitude differences between NGC 6569 stars in the bright and faint red clumps are plotted for each BDBS filter (*ugrizy*) and for the VVV K_S band. The black dots represent the median differences, while the error bars indicate the standard errors based on the dispersion of each population. The solid line indicates the expected differences for each filter based on zero-age HB tracks from the Princeton–Goddard–PUC isochrones (Valcarce, Catelan & Sweigart 2012). The HB tracks were calculated assuming an RGB-tip mass of 0.8 $M_\odot$, $\Delta Y = 0.02$, [Fe/H] = −0.85, [α/Fe] = +0.3, and am HB mass of 0.7 $M_\odot$.

in progressively redder filters. A comparison with theoretical zero-age HB tracks from Valcarce et al. (2012) indicates that the data are relatively consistent with an assumed helium spread of $\Delta Y = 0.02$, as suggested in Johnson et al. (2018). Therefore, we conclude that the red HB split detected by Mauro et al. (2012) is probably real, is marginally detected in the BDBS *z*- and *y*-band data, and that the diminishing magnitude differences in bluer wavelengths can possibly be explained by a small but discrete He abundance spread in the cluster.

4.4.3 FSR 1758

FSR 1758 was originally detected as a probable star cluster in a low-latitude 2MASS search by Froebrich, Scholz & Raftery (2007), but has only recently received significant attention as a possible galaxy nucleus or massive globular cluster (Cantat-Gaudin et al. 2018; Barbá et al. 2019; Simpson 2019; Villanova et al. 2019). Barbá et al. (2019) claimed to detect a large number of extratidal stars, and suggested that FSR 1758 may even be part of a larger extended structure, such as an undiscovered dwarf galaxy. On the other hand, Simpson (2019) noted that many of these extratidal stars are likely foreground dwarfs rather than cluster giants, and Villanova et al. (2019) performed a radial velocity and chemical composition analysis that found FSR 1758 to likely be a monometallic globular cluster. Since BDBS covers a large fraction of the region around FSR 1758, we can provide some additional insight into the presence (or not) of extratidal debris.

Although FSR 1758 is near the edge of the BDBS footprint, Fig. 27 shows that the object is easily detected in our survey. Furthermore, members are readily identified through a combination of broad-band photometry and especially *Gaia* DR2 proper motions. For this paper, we restrict our CMD analysis to the *r* band and redder filters, since FSR 1758 lies outside our reddening map. Redder colours are also generally preferred when searching for extratidal members because Fig. 27 shows that the region near FSR 1758 suffers from significant and highly variable differential reddening.

The *r* versus $r - y$ CMD shown in Fig. 27 indicates that the FSR 1758 RGB is significantly bluer than a majority of the bulge RGB stars, which is consistent with past work suggesting [Fe/H] ∼ −1.5 (Barbá et al. 2019; Villanova et al. 2019). Additionally, we confirm that FSR 1758 has an extended and very blue HB, along with a possible gap in the HB distribution near $y \sim 17$ mag. In this sense, the HB morphology of FSR 1758 closely resembles that of NGC 6656 (e.g. see Fig. 24), including the nearly complete absence of red HB stars. Although differential reddening smears out the RGB colour distribution shown in Fig. 27, the data do not provide any clear evidence supporting a large metallicity spread.

In Fig. 28, we investigate the spatial distribution of stars that may be associated with FSR 1758, especially those outside the tidal radius. Although Fig. 28 shows that FSR 1758's RGB is generally bluer than the bulge sequence, it overlaps enough that cluster RGB stars cannot be readily identified based on their CMD location alone. However, the blue HB stars are well separated from both the bulge RGB and foreground disc sequences, and are therefore more useful

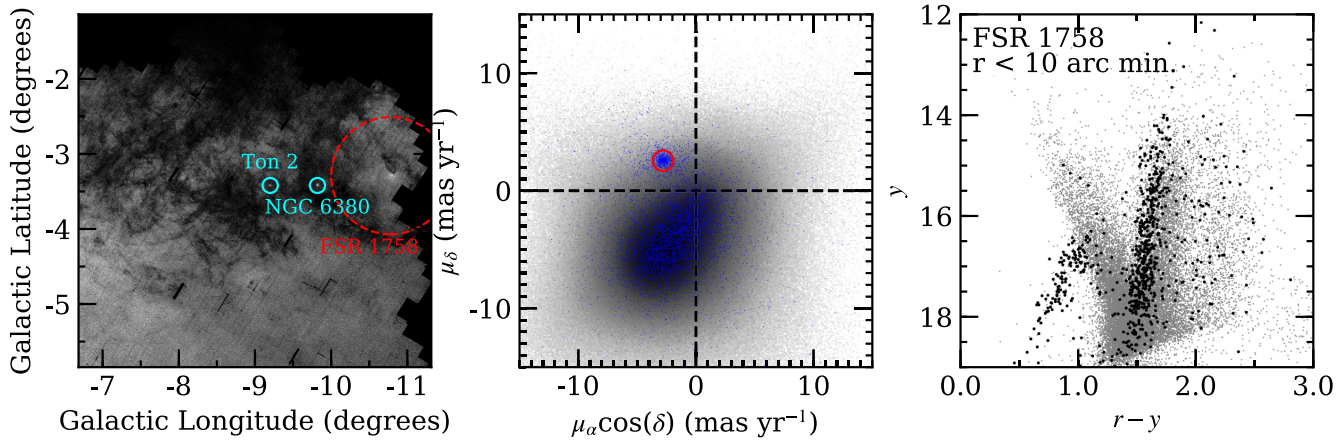

Figure 27. Left: a flux-weighted *r*-band density map of the BDBS region within ∼5° of the massive globular cluster FSR 1758. The 0.78° tidal radius suggested by Barbá et al. (2019) is illustrated by the dashed red line. The nearby but unrelated globular clusters NGC 6380 and Ton 2 are also indicated by the open cyan circles. Middle: a *Gaia* DR2 vector point diagram is shown as a shaded 2D histogram for all objects with proper motion measurements in the left-hand panel. The blue symbols highlight stars with radial distances < 10 arcmin from the cluster centre, and the open red circle indicates the selection criteria used to identify cluster members. Right: a *y* versus $r - y$ CMD is shown for BDBS targets within 10 arcmin of the cluster centre (grey symbols) and for which *Gaia* DR2 proper motions are consistent with cluster membership (black symbols). Note the extended blue HB and gap near $y \sim 17$ that is reminiscent of NGC 6656 (e.g. see Fig. 24).

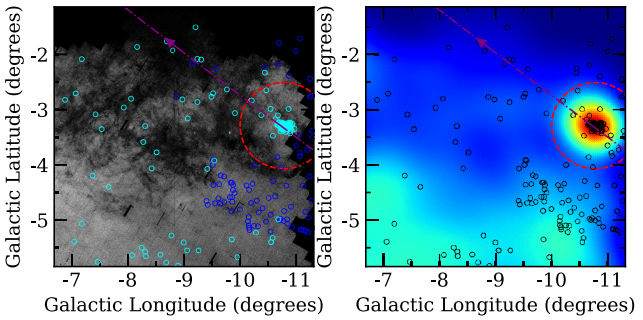

Figure 28. Left: a similar flux-weighted *r*-band density map as shown in Fig. 27 is provided for FSR 1758. The open blue circles indicate possible RGB stars with colours and proper motions consistent with cluster membership, as identified by Barbá et al. (2019). Similarly, the open cyan circles show the locations of blue HB stars identified in the BDBS catalogue that have $r-y$ colours and proper motions consistent with cluster membership. The dotted–dashed purple line and arrow shows the integrated orbit for FSR 1758. Right: a colour gradient map is shown that illustrates the density of all Gaia–BDBS sources with proper motions residing in the cluster selection region of Fig. 27, regardless of a source's colour or luminosity. Bluer shaded colours indicate lower source densities. The open black circles illustrate the positions of all potential RGB and blue HB stars shown in the left-hand panel. Note that a number of blue HB stars lie along the orbit path.

tracers outside the tidal radius. We also utilize *Gaia* DR2 proper motions to remove any remaining bulge blue HB stars that happen to have similar colours/magnitudes to the FSR 1758 HB stars.

The resulting stars with colours, magnitudes, and proper motions consistent with membership in FSR 1758 are identified as cyan open circles in Fig. 28. An obvious clump is found within a few arcminutes of the cluster centre, but the sharp drop-off in blue HB density with radius may indicate that the tidal radius is significantly smaller than the 0.78° reported by Barbá et al. (2019). We do find potential extratidal stars up to several degrees away, but unlike the Barbá et al. (2019) results our potential extratidal stars are distributed throughout the field rather than concentrated in a conspicuous clump.

When we plot the coordinates of all potential extratidal stars over a map showing the density of all *Gaia* DR2 detections that have proper motions matching the FSR 1758 selection region (right-hand panel of Fig. 28), we find that an overwhelming number of the extratidal stars lie in regions where the background contamination is high. A comparison of the two panels in Fig. 28 suggests that the 'low-density' background regions are generally areas with high extinction. Therefore, we find in agreement with Simpson (2019) that most or all of the extratidal stars identified in Barbá et al. (2019) are likely false positives. We do not find any evidence that FSR 1758 is part of a larger structure. However, we do find several possible extratidal members that lie along the leading edge of the cluster's orbit so significant tidal debris may still exist.

5 SUMMARY

BDBS provides *ugrizy* photometry, calibrated on to the SDSS (*u*) and Pan-STARRS (*grizy*) systems, for ∼250 million stars spanning more than 200 sq deg of the Southern Galactic bulge down to depths of ∼22–23 mag. For most fields, the data have already been corrected for reddening using the extinction maps from Simion et al. (2017). This paper describes the tools and methods developed to collate >10 billion detections in ∼450 000 CCD images into a usable catalogue, and also includes some of the first science results from the project. One of the most important discoveries is the tight correlation ($\sigma \sim$ 0.2 dex) between dereddened $u-i$ colour and [Fe/H] for bulge red clump giants. In the future, the derived colour–metallicity relation will be applied to millions of red clump stars, and should prove to be a transformational technique for deriving accurate [Fe/H] values from BDBS data.

For this paper, we applied the red clump colour–metallicity relation to 15 sightlines and found that the bulge is not uniformly bimodal. Fields near $b \sim -4°$ are well fitted by a simple closed box enrichment models that possess a metal-rich peak and a long metal-poor tail. Any additional metal-poor components that might exist are limited to the few per cent level. Exterior bulge fields appear bimodal, and require the addition of a secondary metal-poor population in order to adequately fit their metallicity distributions. However, assuming that the metal-rich peaks in these fields are scaled versions of the $b \sim -4°$ distributions, the long metal-poor tails inherent to the closed box model significantly decreases the strength of the required secondary populations compared to pure Gaussian mixture models.

The BDBS data were further validated using investigations of globular clusters residing in the survey area. For example, we showed that NGC 6626 (blue HB) and NGC 6637 (red HB) are well fitted by isochrones, and that our observations easily reach from the RGB-tip to below the main-sequence turn-off. Standard photometric sequences, such as the AGB and RGB-bump, are also clearly seen. Investigations of NGC 6656 (M 22) also showed that we detect the SGB and RGB splits when using the *u* band, and that the various sequences are driven by metallicity differences. We also searched for extratidal stars and found several candidates up to several degrees away that lie along the orbit path. An analysis of NGC 6569 showed that the split red HB detected in the near-IR by Mauro et al. (2012) is probably real, and that we find marginal detections using the *z* and *y* bands. However, this split HB was restricted to redder colours, which is consistent with a small He abundance spread ($\Delta Y \sim 0.02$). Finally, we used BDBS data to investigate FSR 1758, and found in agreement with past work that the cluster is metal-poor relative to the bulge, has a very blue and extended HB, and is likely a monometallic globular cluster. We find some evidence of extratidal stars lying along the leading path of the cluster's orbit, but do not confirm the existence of a significant tidal debris field. Instead, most of the tidal debris found by Barbá et al. (2019) seems likely to be foreground field stars.

The full BDBS data set will be publicly released soon, and will be a critical community data set for exploring stellar populations within the inner disc and Galactic bulge. The BDBS catalogue will be especially useful when combined with kinematic and imaging surveys operating in other wavelengths. The work presented here offers insight into the types of problems that can be addressed using BDBS, which also serves as a pathfinder for observing strategies and science goals that may be achieved with the Vera C. Rubin Observatory.

ACKNOWLEDGEMENTS

CIJ gratefully acknowledges support from the Clay Fellowship, administered by the Smithsonian Astrophysical Observatory, and thanks Nelson Caldwell for numerous helpful discussions. CIJ and RMR thank Rodrigo Ibata for helpful discussions and early work on the project. CIJ, RMR, WIC, MDY, SM, and CAP acknowledge support by the National Science Foundation (NSF, grant AST-1412673). CAP acknowledges the generosity of the Kirkwood Research Fund at Indiana University. AK gratefully acknowledges funding by the Deutsche Forschungsgemeinschaft (DFG, German Research Foundation) – Project-ID 138713538 – SFB 881 ('The Milky Way System'), subprojects A03, A05, and A11. This research was supported in part by Lilly Endowment, Inc., through its support for the Indiana University Pervasive Technology Institute, and in part by the Indiana METACyt Initiative. The Indiana METACyt

Initiative at IU was also supported in part by Lilly Endowment, Inc. This material is based upon work supported by the National Science Foundation under grant no. CNS-0521433. This work was supported in part by Shared University Research grants from IBM, Inc., to Indiana University. This project used data obtained with the Dark Energy Camera (DECam), which was constructed by the Dark Energy Survey (DES) collaboration. Funding for the DES Projects has been provided by the U.S. Department of Energy, the U.S. National Science Foundation, the Ministry of Science and Education of Spain, the Science and Technology Facilities Council of the United Kingdom, the Higher Education Funding Council for England, the National Center for Supercomputing Applications at the University of Illinois at Urbana-Champaign, the Kavli Institute of Cosmological Physics at the University of Chicago, the Center for Cosmology and Astro-Particle Physics at the Ohio State University, the Mitchell Institute for Fundamental Physics and Astronomy at Texas A&M University, Financiadora de Estudos e Projetos, Fundação Carlos Chagas Filho de Amparo à Pesquisa do Estado do Rio de Janeiro, Conselho Nacional de Desenvolvimento Científico e Tecnológico and the Ministério da Ciência, Tecnologia e Inovação, the Deutsche Forschungsgemeinschaft, and the Collaborating Institutions in the Dark Energy Survey. The Collaborating Institutions are Argonne National Laboratory, the University of California at Santa Cruz, the University of Cambridge, Centro de Investigaciones Enérgeticas, Medioambientales y Tecnológicas-Madrid, the University of Chicago, University College London, the DES-Brazil Consortium, the University of Edinburgh, the Eidgenössische Technische Hochschule (ETH) Zürich, Fermi National Accelerator Laboratory, the University of Illinois at Urbana-Champaign, the Institut de Ciències de l'Espai (IEEC/CSIC), the Institut de Física d'Altes Energies, Lawrence Berkeley National Laboratory, the Ludwig–Maximilians Universität München and the associated Excellence Cluster Universe, the University of Michigan, the National Optical Astronomy Observatory, the University of Nottingham, the Ohio State University, the OzDES Membership Consortium the University of Pennsylvania, the University of Portsmouth, SLAC National Accelerator Laboratory, Stanford University, the University of Sussex, and Texas A&M University. Based on observations at Cerro Tololo Inter-American Observatory, National Optical Astronomy Observatory (2013A-0529; 2014A-0480: RMR), which is operated by the Association of Universities for Research in Astronomy (AURA) under a cooperative agreement with the National Science Foundation.

DATA AVAILABILITY

The raw and pipeline reduced DECam images are available for download on the NOAO archive at http://archive1.dm.noao.edu/. Astrometric, photometric, and reddening catalogues are in the process of being prepared for public release. However, early release may be provided upon request to the corresponding author.

REFERENCES

Alam S. et al., 2015, ApJS, 219, 12
Alves-Brito A., Meléndez J., Asplund M., Ramírez I., Yong D., 2010, A&A, 513, A35
Babusiaux C., 2016, PASA, 33, e026
Babusiaux C. et al., 2010, A&A, 519, A77
Barbá R. H., Minniti D., Geisler D., Alonso-García J., Hempel M., Monachesi A., Arias J. I., Gómez F. A., 2019, ApJ, 870, L24
Barbuy B., Zoccali M., Ortolani S., Hill V., Minniti D., Bica E., Renzini A., Gómez A., 2009, A&A, 507, 405
Barbuy B. et al., 2014, A&A, 570, A76
Barbuy B., Chiappini C., Gerhard O., 2018, ARA&A, 56, 223
Bekki K., 2019, MNRAS, 490, 4007
Bensby T. et al., 2011, A&A, 533, A134
Bensby T. et al., 2013, A&A, 549, A147
Bensby T. et al., 2017, A&A, 605, A89
Cantat-Gaudin T. et al., 2018, A&A, 618, A93
Chambers K. C. et al., 2016, preprint (arXiv:1612.05560)
Clarke J. P., Wegg C., Gerhard O., Smith L. C., Lucas P. W., Wylie S. M., 2019, MNRAS, 489, 3519
Clarkson W. et al., 2008, ApJ, 684, 1110
Clarkson W. I. et al., 2018, ApJ, 858, 46
Currie M. J., Berry D. S., Jenness T., Gibb A. G., Bell G. S., Draper P. W., 2014, in Manset N., Forshay P., eds, ASP Conf. Ser., Vol. 485, Astronomical Data Analysis Software and Systems XXIII. Astron. Soc. Pac., San Francisco, p. 391
Da Costa G. S., Held E. V., Saviane I., Gullieuszik M., 2009, ApJ, 705, 1481
Dékány I., Minniti D., Catelan M., Zoccali M., Saito R. K., Hempel M., Gonzalez O. A., 2013, ApJ, 776, L19
Dotter A., Chaboyer B., Jevremović D., Kostov V., Baron E., Ferguson J. W., 2008, ApJS, 178, 89
Drew J. E. et al., 2014, MNRAS, 440, 2036
Duong L., Asplund M., Nataf D. M., Freeman K. C., Ness M., Howes L. M., 2019, MNRAS, 486, 3586
Ferraro F. R. et al., 2009, Nature, 462, 483
Ferraro F. R., Massari D., Dalessandro E., Lanzoni B., Origlia L., Rich R. M., Mucciarelli A., 2016, ApJ, 828, 75
Flaugher B. et al., 2015, AJ, 150, 150
Freeman K. et al., 2013, MNRAS, 428, 3660
Froebrich D., Scholz A., Raftery C. L., 2007, MNRAS, 374, 399
Fulbright J. P., McWilliam A., Rich R. M., 2007, ApJ, 661, 1152
Gaia Collaboration, 2018a, A&A, 616, A1
Gaia Collaboration, 2018b, A&A, 616, A12
García Pérez A. E. et al., 2013, ApJ, 767, L9
García Pérez A. E. et al., 2018, ApJ, 852, 91
Gilmore G. et al., 2012, The Messenger, 147, 25
Girardi L., Bressan A., Bertelli G., Chiosi C., 2000, A&AS, 141, 371
Gonzalez O. A. et al., 2011a, A&A, 530, A54
Gonzalez O. A., Rejkuba M., Zoccali M., Valenti E., Minniti D., 2011b, A&A, 534, A3
Gonzalez O. A., Rejkuba M., Zoccali M., Valenti E., Minniti D., Schultheis M., Tobar R., Chen B., 2012, A&A, 543, A13
Gonzalez O. A., Rejkuba M., Zoccali M., Valent E., Minniti D., Tobar R., 2013, A&A, 552, A110
Gonzalez O. A. et al., 2015, A&A, 584, A46
González-Fernández C. et al., 2018, MNRAS, 474, 5459
Green G. M. et al., 2018, MNRAS, 478, 651
Hajdu G., Dékány I., Catelan M., Grebel E. K., 2019, Exper. Astron., 49, 217
Hansen C. J., Rich R. M., Koch A., Xu S., Kunder A., Ludwig H. G., 2016, A&A, 590, A39
Harris W. E., 1996, AJ, 112, 1487
Haywood M., Di Matteo P., Snaith O., Calamida A., 2016, A&A, 593, A82
Hewett P. C., Warren S. J., Leggett S. K., Hodgkin S. T., 2006, MNRAS, 367, 454
Hill V. et al., 2011, A&A, 534, A80
Howard C. D. et al., 2009, ApJ, 702, L153
Johnson C. I., Pilachowski C. A., 2010, ApJ, 722, 1373
Johnson C. I., Rich R. M., Fulbright J. P., Valenti E., McWilliam A., 2011, ApJ, 732, 108
Johnson C. I., Rich R. M., Kobayashi C., Fulbright J. P., 2012, ApJ, 749, 175
Johnson C. I., Rich R. M., Kobayashi C., Kunder A., Pilachowski C. A., Koch A., de Propris R., 2013a, ApJ, 765, 157
Johnson C. I., McWilliam A., Rich R. M., 2013b, ApJ, 775, L27
Johnson C. I., Rich R. M., Kobayashi C., Kunder A., Koch A., 2014, AJ, 148, 67
Johnson C. I., Rich R. M., Pilachowski C. A., Caldwell N., Mateo M., Bailey J. I., III, Crane J. D., 2015, AJ, 150, 63
Johnson C. I., Caldwell N., Rich R. M., Mateo M., Bailey J. I., III, Clarkson W. I., Olszewski E. W., Walker M. G., 2017, ApJ, 836, 168

Johnson C. I., Rich R. M., Caldwell N., Mateo M., Bailey J. I., III, Olszewski E. W., Walker M. G., 2018, AJ, 155, 71
Jönsson H., Ryde N., Schultheis M., Zoccali M., 2017, A&A, 598, A101
Joo S.-J., Lee Y.-W., Chung C., 2017, ApJ, 840, 98
Koch A., McWilliam A., Preston G. W., Thompson I. B., 2016, A&A, 587, A124
Kordopatis G. et al., 2013, AJ, 146, 134
Kormendy J., Kennicutt, Robert C. J., 2004, ARA&A, 42, 603
Kunder A. et al., 2012, AJ, 143, 57
Kunder A. et al., 2014, A&A, 572, A30
Kunder A. et al., 2016, ApJ, 821, L25
Kunder A. et al., 2019, ApJ, 877, L17
Lawrence A. et al., 2007, MNRAS, 379, 1599
Lee J. W., López-Morales M., 2007, in Kang Y. W., Lee H. W., Leung K. C., Cheng K. S., eds, ASP Conf. Ser., Vol. 362, The Seventh Pacific Rim Conference on Stellar Astrophysics. Astron. Soc. Pac., San Francisco, p. 279
Lee Y. S. et al., 2008, AJ, 136, 2022
Lee J.-W., 2016, ApJS, 226, 16
Lee Y.-W., Jang S., 2016, ApJ, 833, 236
Lee Y.-W., Joo S.-J., Chung C., 2015, MNRAS, 453, 3906
Lee Y.-W., Hong S., Lim D., Chung C., Jang S., Kim J. J., Joo S.-J., 2018, ApJ, 862, L8
Lee Y.-W., Kim J. J., Johnson C. I., Chung C., Jang S., Lim D., Kang Y., 2019, ApJ, 878, L2
Lewis P. M., Rogers H., Schindler R. H., 2010, in McLean I. S., Ramsay S. K., Takami H., eds, Proc. SPIE Conf. Ser. Vol. 7735, Ground-based and Airborne Instrumentation for Astronomy III. SPIE, Bellingham, p. 77353C
López-Corredoira M., Lee Y. W., Garzón F., Lim D., 2019, A&A, 627, A3
Majewski S. R. et al., 2017, AJ, 154, 94
Marino A. F., Milone A. P., Piotto G., Villanova S., Bedin L. R., Bellini A., Renzini A., 2009, A&A, 505, 1099
Marino A. F. et al., 2011b, ApJ, 731, 64
Marino A. F. et al., 2011a, A&A, 532, A8
Marino A. F. et al., 2012, A&A, 541, A15
Matteucci F., Brocato E., 1990, ApJ, 365, 539
Mauro F., Moni Bidin C., Cohen R., Geisler D., Minniti D., Catelan M., Chené A.-N., Villanova S., 2012, ApJ, 761, L29
Mauro F. et al., 2014, A&A, 563, A76
McWilliam A., 2016, PASA, 33, e040
McWilliam A., Zoccali M., 2010, ApJ, 724, 1491
Meléndez J. et al., 2008, A&A, 484, L21
Mink D. J., 2002, in Bohlender D. A., Durand D., Handley T. H., eds, ASP Conf. Ser., Vol. 281, Astronomical Data Analysis Software and Systems XI. Astron. Soc. Pac., San Francisco, p. 169
Minniti D. et al., 2010, New Astron., 15, 433
Mohammed S., Schiminovich D., Hawkins K., Johnson B., Wang D., Hogg D. W., 2019, ApJ, 872, 95
Mucciarelli A., Lapenna E., Massari D., Pancino E., Stetson P. B., Ferraro F. R., Lanzoni B., Lardo C., 2015, ApJ, 809, 128
Muñoz C. et al., 2018, A&A, 620, A96
Nataf D. M., 2017, PASA, 34, e041
Nataf D. M., Udalski A., Gould A., Fouqué P., Stanek K. Z., 2010, ApJ, 721, L28
Nataf D. M., Udalski A., Gould A., Pinsonneault M. H., 2011, ApJ, 730, 118
Nataf D. M., Cassisi S., Athanassoula E., 2014, MNRAS, 442, 2075
Ness M., Lang D., 2016, AJ, 152, 14
Ness M. et al., 2012, ApJ, 756, 22
Ness M. et al., 2013b, MNRAS, 432, 2092
Ness M. et al., 2013a, MNRAS, 430, 836
Ness M., Asplund M., Casey A. R., 2014a, MNRAS, 445, 2994
Ness M., Debattista V. P., Bensby T., Feltzing S., Roškar R., Cole D. R., Johnson J. A., Freeman K., 2014b, ApJ, 787, L19
Oke J. B., Gunn J. E., 1983, ApJ, 266, 713
Ortolani S., Renzini A., Gilmozzi R., Marconi G., Barbuy B., Bica E., Rich R. M., 1995, Nature, 377, 701
Pietrukowicz P. et al., 2012, ApJ, 750, 169
Pietrukowicz P. et al., 2015, ApJ, 811, 113
Piotto G., 2009, in Mamajek E. E., Soderblom D. R., Wyse R. F. G., eds, IAU Symp., Vol. 258, The Ages of Stars. International Astronomical Union, p. 233
Portail M., Wegg C., Gerhard O., Ness M., 2017, MNRAS, 470, 1233
Price-Whelan A. M., 2017, J. Open Source Softw., 2, 388
Prudil Z., Dékány I., Grebel E. K., Catelan M., Skarka M., Smolec R., 2019, MNRAS, 487, 3270
Renzini A. et al., 2018, ApJ, 863, 16
Rich R. M., 1990, ApJ, 362, 604
Rich R. M., 2013, The Galactic Bulge. Springer, Berlin, p. 271
Rich R. M., Reitzel D. B., Howard C. D., Zhao H., 2007, ApJ, 658, L29
Rich R. M., Origlia L., Valenti E., 2012, ApJ, 746, 59
Rojas-Arriagada A. et al., 2017, A&A, 601, A140
Ryde N., Schultheis M., Grieco V., Matteucci F., Rich R. M., Uttenthaler S., 2016, AJ, 151, 1
Saha A. et al., 2019, ApJ, 874, 30
Saito R. K., Zoccali M., McWilliam A., Minniti D., Gonzalez O. A., Hill V., 2011, AJ, 142, 76
Savino A., Koch A., Prudil Z., Kunder A., Smolec R., 2020, A&A, in press
Schiavon R. P. et al., 2017, MNRAS, 465, 501
Schlafly E. F., Finkbeiner D. P., 2011, ApJ, 737, 103
Schlafly E. F. et al., 2016, ApJ, 821, 78
Schlafly E. F. et al., 2018, ApJS, 234, 39
Schultheis M. et al., 2015, A&A, 584, A45
Schultheis M., Rich R. M., Origlia L., Ryde N., Nandakumar G., Thorsbro B., Neumayer N., 2019, A&A, 627, A152
Searle L., Zinn R., 1978, ApJ, 225, 357
Shen J., Rich R. M., Kormendy J., Howard C. D., De Propris R., Kunder A., 2010, ApJ, 720, L72
Simion I. T., Belokurov V., Irwin M., Koposov S. E., Gonzalez-Fernandez C., Robin A. C., Shen J., Li Z. Y., 2017, MNRAS, 471, 4323
Simpson J. D., 2019, MNRAS, 488, 253
Skrutskie M. F. et al., 2006, AJ, 131, 1163
Soszyński I. et al., 2014, Acta Astron., 64, 177
Soto M., Rich R. M., Kuijken K., 2007, ApJ, 665, L31
Stetson P. B., 1987, PASP, 99, 191
Stetson P. B., 1990, PASP, 102, 932
Surot F. et al., 2019, A&A, 623, A168
Udalski A., Szymański M. K., Szymański G., 2015, Acta Astron., 65, 1
Uttenthaler S., Schultheis M., Nataf D. M., Robin A. C., Lebzelter T., Chen B., 2012, A&A, 546, A57
Valcarce A. A. R., Catelan M., Sweigart A. V., 2012, A&A, 547, A5
Valdes F., Gruendl R., DES Project, 2014, in Manset N., Forshay P., eds, ASP Conf. Ser., Vol. 485, Astronomical Data Analysis Software and Systems XXIII. Astron. Soc. Pac., San Francisc, p. 379
Valenti E., Origlia L., Rich R. M., 2011, MNRAS, 414, 2690
Valenti E., Zoccali M., Renzini A., Brown T. M., Gonzalez O. A., Minniti D., Debattista V. P., Mayer L., 2013, A&A, 559, A98
Van der Swaelmen M., Barbuy B., Hill V., Zoccali M., Minniti D., Ortolani S., Gómez A., 2016, A&A, 586, A1
Villanova S., Moni Bidin C., Mauro F., Munoz C., Monaco L., 2017, MNRAS, 464, 2730
Villanova S., Monaco L., Geisler D., O'Connell J., Minniti D., Assmann P., Barbá R., 2019, ApJ, 882, 174
Wegg C., Gerhard O., 2013, MNRAS, 435, 1874
Zasowski G. et al., 2019, ApJ, 870, 138
Zoccali M. et al., 2003, A&A, 399, 931
Zoccali M. et al., 2006, A&A, 457, L1
Zoccali M., Hill V., Lecureur A., Barbuy B., Renzini A., Minniti D., Gómez A., Ortolani S., 2008, A&A, 486, 177
Zoccali M. et al., 2014, A&A, 562, A66
Zoccali M. et al., 2017, A&A, 599, A12

This paper has been typeset from a TEX/LATEX file prepared by the author.